Where to treat the ground: optimal placement and coverage of reflective ground treatment in bifacial photovoltaic plants

Muhammad Usama[a,*], Muhammad Abdullah Zafar Ghauri[b], Jake Bendetti[a], Moiz Ahmed Mahesar[a], Omer Emre Tunca[a], Yetkin Yildirim[c]

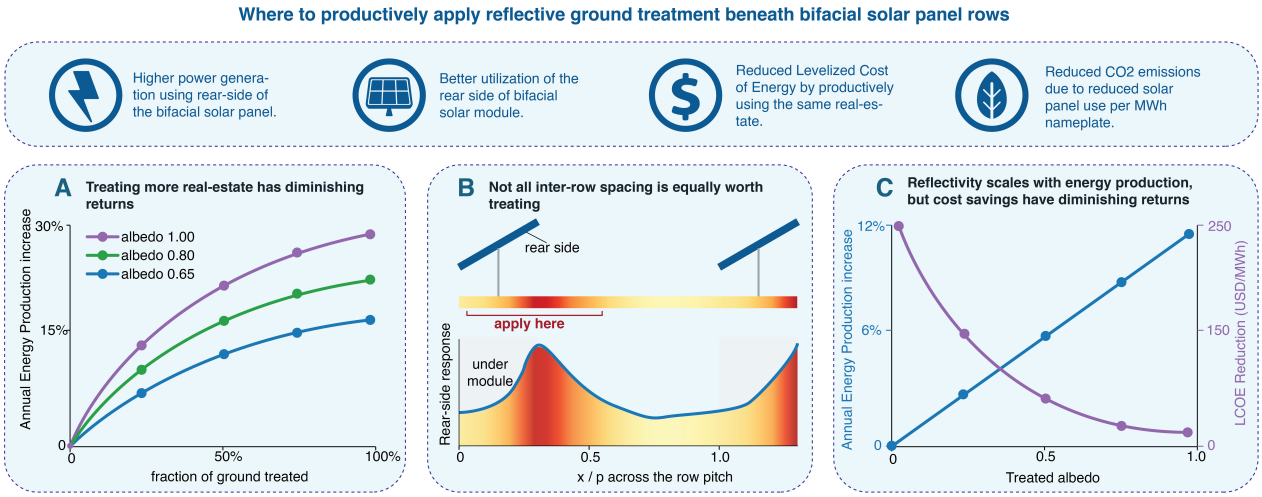
[a] *University of Texas at Austin, Austin, TX, United States*
[b] *National University of Science and Technology (NUST), Pakistan*
[c] *Rice University, Houston, TX, United States*

Abstract

Reflective ground treatment can increase the rear-side irradiance and energy yield of bifacial photovoltaic plants, but its economic value depends on where it is installed and how its performance and costs evolve over time. This study evaluates ground treatment as a capital investment, accounting for installation cost, reflectance degradation, reapplication and avoided vegetation-management expenditure. A view-factor irradiance model is extended to spatially varying ground albedo. Because irradiance incident on the ground is independent of its reflectance, ground-to-module transfer remains exactly linear in segment radiosity, and the spatial formulation reduces identically to the verified uniform-albedo model. The model reproduces a published fixed-tilt benchmark with normalised root-mean-square errors of 0.026% and 0.108% for front- and rear-side irradiance, respectively, and reproduces measured annual bifacial gain at a Danish test facility to 0.037 percentage points, with a mean absolute error of 0.392 percentage points across the eight months for which the comparison is valid.

A 1 MW fixed-tilt plant near Dallas-Fort Worth, Texas, quantifies the energy and economic effects of treatment placement. Annual rear-side response varies by a factor of 3.9 across the row pitch, so treating the most responsive half of the ground captures 65% of the available benefit against 50% for uniform application at equal cost. Because cost scales strictly with treated area while benefit is concave in coverage, the value-maximising coverage is set by the ratio of unit cost to contract price. At $2.25\ \mathrm{USD\,m^{-2}}$ and $45\ \mathrm{USD\,MWh^{-1}}$ the last increment of ground still repays itself, so value is maximised at full coverage of the inter-row pitch, giving a 15.2% annual energy gain at an incremental levelised cost of $32\ \mathrm{USD\,MWh^{-1}}$. At $3.00\ \mathrm{USD\,m^{-2}}$ the optimum falls to 58% of the pitch. Energy gain is linear in treated albedo, yielding break-even reflectances of 0.50 at full coverage and 0.36 for a narrow band beside the rows. Reflectance and placement are therefore substitutes, and specifying treatment reflectance is more important than maximising treated area.

Graphical Abstract



Keywords: bifacial photovoltaics; ground albedo; techno-economic assessment; levelised cost of electricity; view-factor model; albedo enhancement

*Corresponding author: Muhammad Usama. Email: mu3854@my.utexas.edu

Nomenclature

Symbol	Description, unit
Solar position and orientation	
$\theta_{z,t}$	Solar zenith angle, deg
$\gamma_{s,t}$	Solar azimuth, south-referenced, positive west, deg
$\alpha_{s,t}$	Solar elevation angle, deg
$\beta_{q,t}$	Tilt of face q from horizontal, deg
$\gamma_{q,t}$	Surface azimuth of face q, south-referenced, deg
$\theta_{q,t}$	Solar incidence angle on face q, deg
n_{doy}	Day of year
Array geometry	
L_m	Module slant length, m
W_m	Module width, m
C	Ground clearance of the lower module edge, m
D	Horizontal gap between adjacent row projections, m
p	Row pitch, $D + L_m \cos\beta_F$, m
GCR	Ground-coverage ratio, L_m/p
N_q	Module-face elements per face
N_g	Inter-row ground segments per pitch
N_ψ	Angular sectors per module element
ψ_m	Sector bound, measured from the module plane, deg
$x_i, \Delta x_i$	Centre and width of ground segment i, m
Irradiance	
$I_{\mathrm{DNI},t}$	Direct normal irradiance, $\mathrm{W\,m^{-2}}$
$I_{\mathrm{DHI},t}$	Diffuse horizontal irradiance, $\mathrm{W\,m^{-2}}$
$I_{\mathrm{GHI},t}$	Global horizontal irradiance, $\mathrm{W\,m^{-2}}$
I_{STC}	Standard test condition irradiance, 1000, $\mathrm{W\,m^{-2}}$
I_{sc}	Solar constant, 1367, $\mathrm{W\,m^{-2}}$
$I_{\mathrm{beam},q,j,t}$	Direct beam on element j of face q, $\mathrm{W\,m^{-2}}$
$I_{\mathrm{sky},q,j,t}$	Diffuse sky contribution, $\mathrm{W\,m^{-2}}$
$I_{\mathrm{grd},q,j,t}$	Ground-reflected contribution, $\mathrm{W\,m^{-2}}$
$I_{\mathrm{nb},q,j,t}$	Neighbouring-row reflected contribution, $\mathrm{W\,m^{-2}}$
$I_{\mathrm{cir},q,t}$	Circumsolar component, $\mathrm{W\,m^{-2}}$
$I_{\mathrm{therm},t}$	Total absorbed irradiance, $\overline{I}_F + \overline{I}_R$, $\mathrm{W\,m^{-2}}$
$I_{\mathrm{eff},t}$	Effective bifacial irradiance, $\mathrm{W\,m^{-2}}$
$\overline{I}_{q,t}$	Area-averaged irradiance on face q, $\mathrm{W\,m^{-2}}$
$G_{i,t}$	Irradiance incident on ground segment i, $\mathrm{W\,m^{-2}}$
$J_{i,t}$	Radiosity of ground segment i, $\rho_i G_i$, $\mathrm{W\,m^{-2}}$
H_q	Annual irradiation on face q, $\mathrm{kWh\,m^{-2}}$
H_{eff}	Annual effective bifacial irradiation, $\mathrm{kWh\,m^{-2}}$
Sky model and optics	
ε_t	Perez sky-clearness parameter
κ_ε	Perez clearness constant, 1.041
Δ_t	Perez sky-brightness parameter
$F_{1,t}, F_{2,t}$	Circumsolar and horizon-brightening coefficients
$f_{11} \ldots f_{23}$	Perez all-sites-composite coefficients
AM_t	Relative optical air mass
b_t	Circumsolar projection denominator
IAM	Incidence-angle modifier
n_g	Cover refractive index, 1.526
R_0	Normal-incidence reflectance
R_s, R_p	Fresnel reflectances, perpendicular and parallel
ΔCF_m	Configuration-factor weight of sector m
$\mathrm{VF}_{q_j \to g_i}$	View factor, element j of face q to segment i
$\mathrm{VF}_{g_i \to \mathrm{sky}}$	Sky view factor of ground segment i

Symbol	Description, unit
$s_{q,j,t}$	Shaded fraction of element j on face q
$u_{i,t}$	Sunlit fraction of ground segment i
τ	Module transmission factor onto shaded ground
Ground treatment	
$\rho_{i,t}$	Albedo of ground segment i
ρ_{base}	Natural, untreated ground albedo
ρ_{treated}	Treated ground albedo
$\rho^{\min}$	Break-even treated albedo
χ_i	Treated fraction of ground segment i
Ω	Union of treated intervals across the row pitch
f_{cov}	Treated fraction of the row pitch
A_{treated}	Treated ground area, $\mathrm{m^2}$
$M_{q,i}$	Annual response of face q to unit albedo on segment i, $\mathrm{kWh\,m^{-2}}$
$\mathcal{K}$	Annual gain per unit treated area per unit albedo, $\mathrm{kWh\,m^{-2}}$
k_t	Reflectance decay factor in year t
ξ_t	Fraction of vegetation cost displaced in year t
Energy and plant	
P_{rated}	Rated direct-current plant capacity, kW
η_{module}	Module efficiency at STC
φ_{bif}	Module bifaciality factor
$\gamma_{P_{\mathrm{mp}}}$	Module power temperature coefficient, $\%\,^\circ\mathrm{C^{-1}}$
T_{NOCT}	Nominal operating cell temperature, °C
$T_{\mathrm{cell},t}, T_{\mathrm{amb},t}$	Cell and ambient temperature, °C
v_t	Wind speed, $\mathrm{m\,s^{-1}}$
$f_{\mathrm{temp},t}$	Temperature correction factor
$f_{\mathrm{opt},q}, f_{\mathrm{mis},q,t}$	Side-specific optical and mismatch factors
L_{sys}	Lumped system losses
d	Annual module degradation rate, $\mathrm{yr^{-1}}$
AEP	Annual energy production, kWh
$A_{\mathrm{panels}}, A_{\mathrm{farm}}$	Module and total plant area, $\mathrm{m^2}$
LUI	Land-use intensity, $\mathrm{acres\,MW^{-1}}$
Economics	
r	Discount rate (WACC)
n	Project lifetime, yr
e	Electricity price escalation rate
$P_{\mathrm{elec},t}$	Contract electricity price in year t, $\mathrm{USD\,kWh^{-1}}$
$c_{\mathrm{material}}, c_{\mathrm{labour}}$	Treatment material and application unit cost, $\mathrm{USD\,m^{-2}}$
c_{veg}	Vegetation-management cost per treated area, $\mathrm{USD\,m^{-2}\,yr^{-1}}$
C_{spray}	Upfront treatment capital expenditure, USD
t_{reapp}	Reapplication interval, yr
N_{reapp}	Number of reapplications over the project life
$\mathrm{TCC}_{\mathrm{base}}$	Baseline total capital cost, USD
AOE	Annual operating expense, $\mathrm{USD\,yr^{-1}}$
$\Delta\mathrm{AOE}_t$	Avoided annual operating expense, $\mathrm{USD\,yr^{-1}}$
CRF	Capital recovery factor, $\mathrm{yr^{-1}}$
S	Discounted revenue factor, $\mathrm{USD\,kWh^{-1}}$
CF_t	Net incremental cash flow in year t, USD
LCOE	Levelised cost of electricity, $\mathrm{USD\,MWh^{-1}}$
LCOE_Δ	Incremental levelised cost of the treatment, $\mathrm{USD\,MWh^{-1}}$
NPV	Net present value %
IRR, MIRR	Internal and modified rate of return, USD
NOCT	Nominal operating cell temperature

1. Introduction

Bifacial photovoltaic (PV) modules, which convert sunlight incident on both the front and rear surfaces of the cell, have moved from a niche technology to a module architecture in utility-scale solar deployment [1, 2]. For a comparable manufacturing cost to monofacial modules, a bifacial module can effectively harvest albedo irradiance on its rear face in addition to the direct and diffuse irradiance on its front face. This rear contribution adds to the annual energy yield without a proportional increase in land and equipment cost [3]. This additional energy is governed by the reflectivity of the ground beneath and between module rows, together with mounting geometry, including tilt angle, elevation, row spacing, and tracking configuration [4, 5]. These parameters determine the extent of reflected solar radiation reaching the rear surface [6, 7, 8]. Under the natural ground conditions typical of most utility-scale sites, such as grass, bare soil or light vegetation with the albedo in the range of 0.15-0.25, the resulting bifacial gain is modest. Field measurements across a wide range of climates tend to converge on a similar order of magnitude. Almarshoud et al. [9] indicated 3.5-7.0% greater energy efficiency and 4.5-9.5% enhanced exergy efficiency compared to monofacial modules under cloudy conditions in Saudi Arabia. Baloch et al. [10] reported 16.3% more energy generation for bifacial PV arrays compared to monofacial panels in Qatar, with module temperature depending on the temporal distribution of albedo radiation. Grommes et al. [11] reported a slight gain for fixed-tilt installations in Germany, and Ghafiri et al. [12] observed 8.4-11.7% bifacial gain for a fixed-tilt system in Sherbrooke, Canada. Garrod et al. [13] analyzed the thermo-electrical properties of bifacial PV panels subjected to variable albedo conditions in the United Kingdom. Global simulations and field measurements indicate that bifacial gain is typically limited to approximately 5-10% over ordinary soil or vegetation. Substantially larger gains generally require higher-albedo ground treatments, often combined with sufficient module elevation and favorable array geometry [14, 15].

A wide range of literature has tested this proposition by evaluating ground albedo with artificial or reflective materials. At NREL's (now Rockies) bifacial experimental single-axis tracking (BEST) field in Colorado, high-density-polyethylene ground reflectors with approximately 70% solar-weighed reflectivity increased the daily energy yield by 6.2% relative to natural albedo [16]. Riedel et al. [17] evaluated the electrical performance and economic value of 6-parallel 13 kWp monofacial and bifacial arrays,with horizontal single-axis trackers (HSAT) and 25° fixed-tilt structure, under low and high albedo configurations. The study found an average of 25% improvement in total energy gain on the tracker fitted with white ground cloth. The ground albedo enhancement produces only a modest LCOE reduction, and the uncertainty in the upfront and ongoing cost of altering large areas of ground makes the approach unadvisable at utility scale. Related agrivoltaic modeling work has shown that the choice of albedo representation, such as fixed, satellite-based or dynamically measured, materially changes the predicted irradiance and power output [18, 19].

The economics of any ground-treatment intervention are further complicated by the diversity of mounting configurations extensively deployed at utility scale. Bifacial gain, land-use intensity and the marginal value of rear irradiance vary substantially between fixed-tilt, single-axis tracked (SAT), dual-axis tracked, and vertical east-west installations [20, 21]. Combining bifacial modules with single-axis tracking has shown a substantial reduction in LCOE by 16% and an increase in energy yield by 35% compared to monofacial fixed-tilt systems, with the bifacial-plus-SAT combination achieving the lowest LCOE across 93.1% of the world's total area [1]. Chudinzow et al. [22] conducted a continent-scale study of 12 European locations and found that vertical bifacial plants result in a higher LCOE than fixed-tilt alternatives, but can outperform them at latitudes greater than 50°. Badran et al. [23] conducted a full-year empirical study in the United Kingdom and measured a vertical heterojunction bifacial system outperforming an equivalent tilted monofacial system by 22.9-26.9%. [24] indicated approximately 82% yield of vertical bifacial systems against horizontally-inclined systems, while offering better self-cleaning and shading tolerances. Because ground coverage ratio, row spacing, and optimal tilt spacing interact differently with each configuration [7], and because land-use intensity itself varies from 2.8 to 4.2 acres per installed megawatt across 736 empirically surveyed US plants [25], a ground-treatment strategy that is economically attractive for one configuration cannot be assumed to be suitable for another without re-evaluation.

A System Advisor Model-based assessment of fixed, single and dual-axis bifacial systems across six deserts worldwide found average specific yields of 2040-2555 kWh/kWp and LCOE as low as 2.45 cents/kWh under desert conditions [26]. Mandy et al. [27] indicated that PV electricity costs for smallest-scale PV systems as £149/MWh and £51/MWh for large-scale systems, with predicted 40-50 %price reductions by 2035. In China, [28] demonstrated that the optimal choice between tracking and fixed-tilt technology depends on local land prices. Since tracking system generates more electricity per unit capacity but require substantially more land, whereas fixed-tilt systems minimize land occupation. Ahmad et al. [29] performed a techno-economic assessment of grid-connected PV in Punjab and demonstrated internal rates of return exceeding 14% and LCOE of 8.5¢/kWh using conservative fixed-tilt assumptions. Desert deployment introduces durability concerns for any ground treatment extensively used for existing PV techniques. Hossain et al. [30] indicated that anti-soiling coatings in the Middle East and North Africa must compete with dust-driven power losses that reach 1% per day. Taquichiri et al. [31] conducted a year-long field study in the Atacama Desert and found that fixed-tilt bifacial modules accumulate approximately 30% more front-surface dust than tracked systems. The study further reported that wetting-and-drying cycles form cemented soiling layers that are substantially harder to remove than loose dust. Reliability considerations extend to the module side of the system as well. With scaled bifacial deployment, potential-induced degradation (PID) has emerged as a risk since both the front and rear surfaces are exposed to degradation pathways. These include shunting, polarization, sodium-ion migration and corrosion-type PID that previously affected only the

front side of the module [32].
Despite the extensive literature on bifacial photovoltaic performance and ground albedo improvement, several crucial research gaps remain unsolved. Existing investigations have focused on energy yield benefits of high-albedo artificial or reflective materials under uniform ground conditions, while little attention has been given to evaluating ground treatments as comprehensive capital investments. Moreover, although the optical mechanisms of bifacial gain are widely documented, no model jointly treats ground-albedo enhancement alongside installation costs, reflectance degradation, reapplication schedules and specific operational savings derived from vegetation management. Furthermore, a systematic techno-economic framework that models a spatially non-uniform ground albedo to optimize the physical placement of reflective materials is absent from literature. As a result, the economic trade-offs between coverage area, produce reflectance and optimal material placement have bot been systematically established for utility-scale bifacial plants. The principal novelties of the following investigation are summarized as follows:

- Development of an extended view-factor irradiance model capable of resolving spatially varying ground albedo, proving that the transfer to the module is exactly linear in segment radiosities.
- First comprehensive techno-economic demonstration that the inter-row ground is not uniform and worth treating, and that applying materials in descending order of optical response captures a disproportionate share of available energy benefit.
- Establishment of a financial framework that evaluates the treatment as a standalone capital investment, and identification of the cost-to-price ratio at which the value-maximizing coverage moves from the full row pitch to an interior fraction.
- Comprehensive quantitative derivation of a closed-form threshold for break-even reflectance, identifying the minimum performance based on cost, placement and system economics.
- Demonstration that product reflectance and physical placement serve as economic substitutes, implying that specifying the reflectance of a product is more significant that specifying the overall areas covered.

The primary objectives of the present investigation are to extend an established view-factor irradiance model to account for spatially varying ground albedo across the inter-row pitch, to develop and implement a coupled techno-economic model that integrates ground treatment capital costs, reflectance degradation, and avoid vegetation management expenses. The study also aims to evaluate the spatial distribution of rear-side energy response to determine the optimal placement of reflective materials and to investigate the economic trade-offs between treatment coverage fraction and treated albedo through detailed discounted cash-flow analysis. In the end, the research aims to establish a robust computational framework that provides actionable procurement thresholds, such as break-even treated albedo, for utility-scale bifacial photovoltaic installations.

2. Techno-economic Assessment Model

The techno-economic assessment (TEA) links the bifacial irradiance model, energy-yield model, ground-treatment cost model, and discounted cash-flow financial model into a single internally consistent framework. The model is organized around a single physical mechanism, implying that increasing the albedo of the ground beneath and between module rows increases the irradiance reaching the rear face of a bifacial module. Consequently, the annual energy production increases, which influences the project's levelized cost of electricity (LCOE), net present value (NPV), internal rate of return (IRR) and payback period compared to an untreated baseline. The downstream quantities, including energy yield, land area, treatment cost, and financial metrics, are evaluated twice for each scenario (ground-treated and control). These scenarios include the site's natural ground albedo and the elevated albedo achieved by reflective treatment.

The irradiance and energy-yield components draw on the established bifacial modeling. This includes the configuration-factor formulation of Marion et al. [33], the ground-reflected irradiation model developed by Sun et al. [14], the view factor formulation developed by Appelbaum et al. [34], the anisotropic diffuse sky-model of Perez et al. [35], the Fresnel angle-of-incidence correction used by the reference implementation [33] with the angular reflection-loss model of Martin et al. [36] available as an alternative, and the general radiative-transfer and thermal framework of Duffie et al. [37]. While the physics of bifacial gain and the economics of utility-scale solar are extensively studied in the literature, no published model jointly treats ground-albedo enhancement as a capital investment with its own installation cost, degradation and reapplication costs, and the savings in operational cost due to suppression of vegetation. The financial parameters, including capital recovery, levelized cost of electricity (LCOE), discounted cash flow, net present value (NPV), and internal rate of return (IRR), follow standard corporate-finance and NREL (now Rockies) techno-economic methodology [38, 39].

The model is implemented in the view-factor and shading routines of the NREL `bifacialvf` reference code [33, 40], with the ground reflection generalized as described in Section 2.1.3. Its verification against the published fixed-tilt benchmark, together with the numerical convergence and internal consistency checks, is reported separately in Section 3.

2.1. *Bifacial Irradiance Model*

The irradiance model resolves the plane-of-array irradiance on both module faces at hourly resolution, with the inter-row ground discretized so that albedo may vary along the row pitch as shown in Figure 1. It follows the view-factor formulation of Marion et al. [33], with ground-reflected irradiance treated as in Sun et al. [14] and Appelbaum [34], diffuse sky irradiance from the anisotropic Perez model [41, 35], and the general radiative framework of Duffie and Beckman [37]. Only the ground-reflection step departs from the reference formulation, and that departure is exact in the sense established in Section 2.1.3.

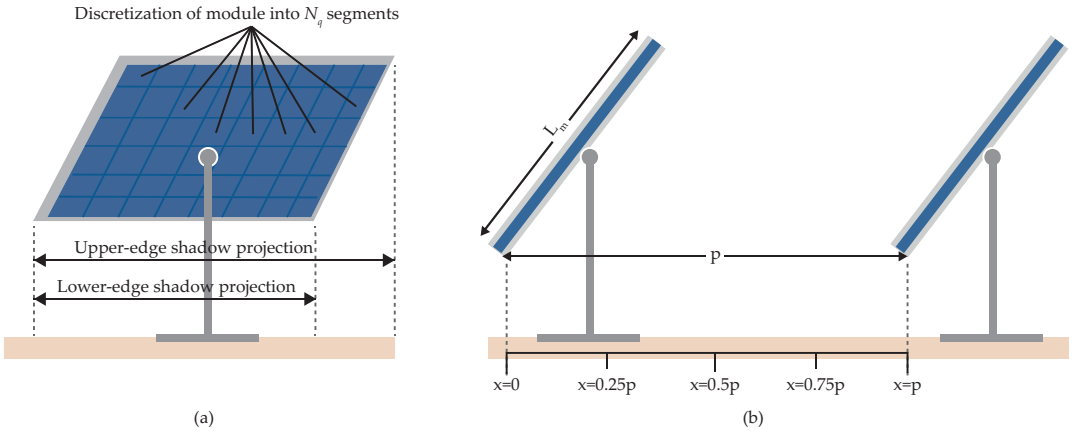


Figure 1: Discretization of the module and the ground. (a) Rear side of the PV module discretized into multiple segments, (b) Inter-row spacing of length equal to pitch p discretized from $x/p = 0.0$ to $x/p = 1.0$

Throughout, $q \in \{F, R\}$ denotes the module face, with F the front and R the rear surface; j indexes an element on face q; i indexes a ground segment; and t indexes the simulation timestep. Table 1 and Figure 2(a) define the angular quantities, and Figure 2(b) shows the radiation components resolved by the model.

Table 1: Solar-position and module-orientation quantities.

Symbol	Quantity	Definition
$\theta_{z,t}$	Solar zenith angle	Angle between the direction toward the Sun and the upward vertical.
$\gamma_{s,t}$	Solar azimuth angle	Angle between true south and the horizontal projection of the direction toward the Sun; negative east of south, positive west of south.
$\beta_{q,t}$	Oriented surface tilt	Angle between the outward normal of face q and the upward vertical. Fixed-tilt arrays have $\beta_{q,t} = \beta_q$.
$\gamma_{q,t}$	Surface azimuth	Angle between true south and the horizontal projection of the outward normal to face q.
$\theta_{q,t}$	Surface incidence angle	Angle between the direction toward the Sun and the outward normal to face q, defined over $0° \leq \theta \leq 180°$.

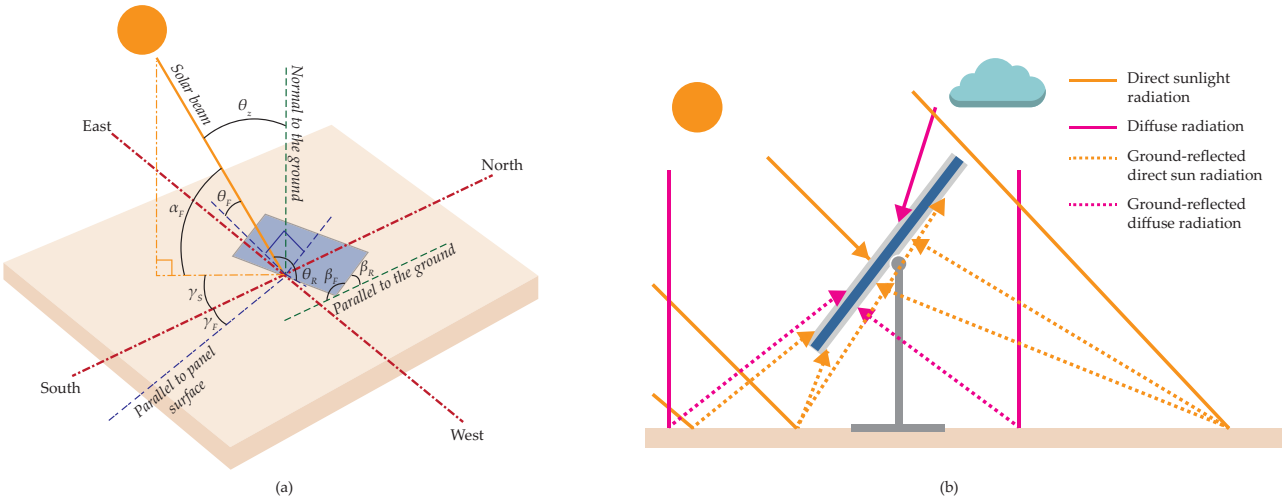


Figure 2: (a) Solar-position and bifacial-module orientation angles used to calculate irradiance on the front and rear surfaces. (b) Side view of one row showing the direct, diffuse and ground-reflected components incident on the front and rear faces.

2.1.1. *Array geometry and incidence angles*

The front and rear surfaces of a bifacial module are coplanar with oppositely directed outward normals, such that

$$\beta_R = 180^\circ - \beta_F, \qquad \gamma_R = (\gamma_F + 180^\circ) \bmod 360^\circ. \tag{1}$$

The incidence angle on either face follows from

$$\cos\theta_{q,t} = \cos\theta_{z,t}\cos\beta_{q,t} + \sin\theta_{z,t}\sin\beta_{q,t}\cos\left(\gamma_{s,t} - \gamma_{q,t}\right), \qquad q \in \{F, R\}, \tag{2}$$

from which $\cos\theta_{R,t} = -\cos\theta_{F,t}$ for an ideal coplanar module. This does not assign either face a permanently sun-facing role. It states that at any timestep a direct ray can illuminate only the face whose outward normal has a positive projection toward the Sun, which the model enforces by evaluating the projected beam term as $\max(0, \cos\theta_{q,t})$. The formulation therefore applies without modification to tilted, vertical east-west, and tracking configurations, for which $\beta_{q,t}$ and $\gamma_{q,t}$ are re-evaluated at each timestep.

As illustrated in Figure 3, the array geometry is expressed in units of the module slant length L_m. The ground clearance of the lower module edge is C, the horizontal gap between the projected edges of adjacent rows is D, and the row pitch is $p = D + L_m\cos\beta_F$. The geometry is solved in these normalised units and lengths are restored by multiplying by L_m before any area is computed.

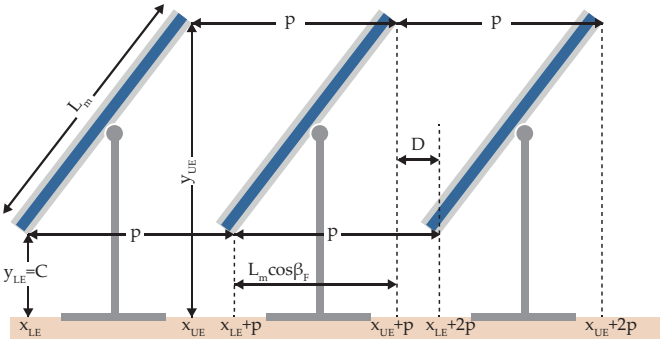


Figure 3: Row configuration in the vertical cross-section normal to the rows, showing the module slant length L_m, front tilt β_F, lower-edge ground clearance C, horizontal gap between adjacent rows D, and the resulting row pitch p.

2.1.2. *Plane-of-array irradiance*

The irradiance on element j of face q is cumulative sum of three contributions,

$$I_{q,j,t} = I_{\mathrm{beam},q,j,t} + I_{\mathrm{sky},q,j,t} + I_{\mathrm{grd},q,j,t}, \qquad q \in \{F, R\}, \tag{3}$$

each shown in Figure 2(b) and each reduced by obstruction from the neighbouring rows. The obstruction is handled by two distinct mechanisms. The direct beam arrives from a single direction, so obstruction is a shadow test that returns the shaded fraction of the element. Everything else arrives from across the outward hemisphere, so obstruction is resolved by partitioning that hemisphere once and asking, for each direction, what surface lies at the other end? The partition is described first, because the sky, ground and neighbouring-row terms are all interpreted from it.

Angular discretisation and surface visibility

The outward hemisphere of each module element is divided into N_ψ angular sectors of width $\Delta\psi$, sector m spanning ψ_m to ψ_{m+1} measured from the plane of the module. Sector m carries the configuration-factor weight

$$\Delta CF_m = \tfrac{1}{2}\left(\cos\psi_m - \cos\psi_{m+1}\right), \tag{4}$$

which is the fraction of the element's radiative exchange associated with that range of directions. The weights are largest near the surface normal and smallest at grazing incidence. As shown in Figure 4, a ray is cast along each sector and assigned to the first surface it intersects. Every sector therefore falls into exactly one of three sets: it reaches the sky without obstruction ($\mathcal{M}_{\mathrm{sky}}$), it terminates on inter-row ground segment i ($\mathcal{M}_i$), or it terminates on the facing surface of a neighbouring row ($\mathcal{M}_{\mathrm{nb}}$). These sets are disjoint and exhaust the hemisphere, so that

$$\sum_{m\in\mathcal{M}_{\mathrm{sky}}} \Delta CF_m + \sum_{i=1}^{N_g}\sum_{m\in\mathcal{M}_i} \Delta CF_m + \sum_{m\in\mathcal{M}_{\mathrm{nb}}} \Delta CF_m = \sum_{m=1}^{N_\psi} \Delta CF_m = 1. \tag{5}$$

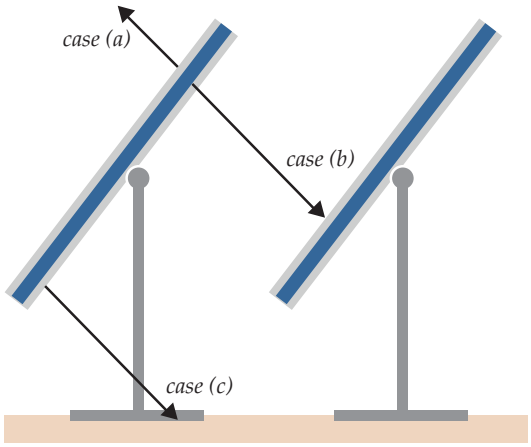


Figure 4: Ray cast from each discretized control surface from both surfaces of the solar PV module. Case (a): Ray cast from surface not intersecting anything, Case (b): Ray cast from surface intersecting another PV module, Case (c): Ray cast from surface intersecting the ground.

Equation (5) is a partition of unity over the three possible destinations. It guarantees that no direction is counted twice and none is omitted, and it is asserted numerically as an implementation check (Section 3).

The view factors used in the following paragraphs are simply the weights accumulated over each set,

$$\mathrm{VF}_{q_j\to\mathrm{sky}} = \sum_{m\in\mathcal{M}_{\mathrm{sky}}} \Delta CF_m, \qquad \mathrm{VF}_{q_j\to g_i} = \sum_{m\in\mathcal{M}_i} \Delta CF_m. \tag{6}$$

The sky-view and ground-view factors are therefore not independent quantities obtained from separate constructions;but they are two readings of the same angular sweep. Because the array geometry is fixed, the sweep is performed once and reused at every timestep.

Direct beam irradiance ($I_{\mathrm{beam},q,j,t}$):

The beam irradiance on element j is

$$I_{\mathrm{beam},q,j,t} = (1 - s_{q,j,t})\left[I_{\mathrm{DNI},t}\max\left(0,\cos\theta_{q,t}\right) + I_{\mathrm{cir},q,t}\right]\mathrm{IAM}\left(\theta_{q,t}\right), \tag{7}$$

where $s_{q,j,t} \in [0,1]$ is the fraction of the element shadowed by an adjacent row, so that $s_{q,j,t} = 0$ denotes a fully sunlit element. Because the beam occupies one direction rather than a range of directions, its obstruction is a shadow test and not a sector sum; $s_{q,j,t}$ is recomputed at every timestep from the solar position and row geometry, whereas the angular partition above is fixed.

The circumsolar component $I_{\mathrm{cir},q,t}$ of the Perez decomposition is carried here rather than with the diffuse sky, because it arrives from the solar direction and is therefore subject to the same visibility, shading and incidence-angle conditions as the beam. It is correspondingly excluded from the sky term below, so that it is counted once. Radiation reaching the module is partly reflected at the air-glass interface, increasingly so at oblique incidence. The loss is represented by the normalised Fresnel transmittance for a cover of refractive index $n_g = 1.526$,

$$\mathrm{IAM}(\theta) = \frac{1 - \frac{1}{2}\left[R_s(\theta) + R_p(\theta)\right]}{1 - R_0}, \qquad R_0 = \left(\frac{n_g - 1}{n_g + 1}\right)^2, \tag{8}$$

where R_s and R_p are the Fresnel reflectances of the perpendicular and parallel polarisation components, evaluated with the refraction angle from Snell's law, and the normalisation gives $\mathrm{IAM}(0^\circ) = 1$. The modifier is applied to the beam at its incidence angle $\theta_{q,t}$ as well as every angular sector at its own incidence angle $\theta_{q,j,m}$. Equation (8) is the optical model of the reference this study is verified against [33]; the angular-loss model of Martin and Ruiz [36, 42] may be substituted, and the effect of doing so is quantified in Section 3.

Perez diffuse transposition ($I_{\mathrm{sky},q,t}$):

Diffuse sky radiation is not distributed uniformly over the sky dome. It is concentrated around the solar disc, and under some conditions the region near the horizon is brighter than the rest of the sky. The Perez model [35] represents this by splitting the diffuse horizontal irradiance into isotropic, circumsolar and horizon-brightening parts whose relative weights are re-evaluated at every timestep from the instantaneous sky condition. Two dimensionless parameters describe that condition. The sky-clearness parameter compares the direct and diffuse components,

$$\varepsilon_t = \frac{\left(I_{\mathrm{DHI},t} + I_{\mathrm{DNI},t}\right)/I_{\mathrm{DHI},t} + \kappa_\varepsilon \theta_{z,t}^3}{1 + \kappa_\varepsilon \theta_{z,t}^3}, \qquad \kappa_\varepsilon = 1.041, \tag{9}$$

and rises from unity under fully overcast skies toward large values as the direct beam strengthens. The sky-brightness parameter measures how much diffuse radiation is present relative to the extraterrestrial resource,

$$\Delta_t = \frac{I_{\mathrm{DHI},t}\, AM_t}{I_{\mathrm{sc}}}, \qquad I_{\mathrm{sc}} = 1367\ \mathrm{W\,m^{-2}}, \tag{10}$$

where the relative optical air mass is

$$AM_t = \left[\cos\theta_{z,t} + 0.15\left(93.9^\circ - \theta_{z,t}\right)^{-1.253}\right]^{-1}. \tag{11}$$

Following the reference implementation, Δ_t is normalised by the solar constant rather than by the eccentricity-corrected extraterrestrial normal irradiance. The correction would alter Δ_t by up to 3.3% near perihelion and prevents exact reproduction of the published benchmark, so it is excluded from the verified baseline and its effect is quantified in Section 3.

The value of ε_t assigns each timestep to one of eight clearness bins, each carrying its own set of empirical coefficients f_{11}-f_{23} from the all-sites-composite parameterisation. The circumsolar and horizon-brightening coefficients then follow as

$$F_{1,t} = \max\left[0,\ f_{11} + f_{12}\Delta_t + f_{13}\theta_{z,t}\right], \qquad F_{2,t} = f_{21} + f_{22}\Delta_t + f_{23}\theta_{z,t}, \tag{12}$$

with $\theta_{z,t}$ in radians in Eqs. (9) and (12). The coefficient $F_{1,t}$ sets how much diffuse radiation is drawn into the circumsolar region and grows as the sky clears. The coefficient $F_{2,t}$ is a correction relative to the isotropic baseline and may be negative; a negative value indicates that the horizon band contributes less than a uniformly bright sky would, not that it contributes nothing.

For an unobstructed face the three components combine to the familiar closed form

$$I_{\mathrm{sky},q,t}^{\mathrm{unob}} = I_{\mathrm{DHI},t}\left[\left(1 - F_{1,t}\right)\frac{1 + \cos\beta_{q,t}}{2} + F_{1,t}\frac{\max\left(0, \cos\theta_{q,t}\right)}{b_t} + F_{2,t}\sin\beta_{q,t}\right], \tag{13}$$

where $\beta_{q,t}$ is the tilt of face q, $\theta_{q,t}$ the corresponding incidence angle, and

$$b_t = \max\left[\cos 85^\circ,\ \cos\theta_{z,t}\right] \tag{14}$$

bounds the circumsolar projection near sunrise and sunset, where $\cos\theta_{z,t} \to 0$ would otherwise make the term diverge.

Within an array the sky is visible only through the sectors in $\mathcal{M}_{\mathrm{sky}}$, so the isotropic term is accumulated over those sectors with their individual incidence-angle modifiers, and the horizon term is scaled by the visible fraction $v_{\mathrm{hor},q,j,t}$ of the horizon band:

$$I_{\mathrm{sky},q,j,t} = I_{\mathrm{DHI},t}\left[\left(1 - F_{1,t}\right)\sum_{m \in \mathcal{M}_{\mathrm{sky}}} \Delta CF_m\, \mathrm{IAM}(\theta_{q,j,m}) + F_{2,t}\, v_{\mathrm{hor},q,j,t}\sin\beta_{q,t}\right]. \tag{15}$$

The circumsolar term is absent because it is carried in Eq. (7). Removing the neighbouring rows sends $\mathcal{M}_{\mathrm{sky}}$ to the whole upward hemisphere, so that the summation tends to $\left(1 + \cos\beta_{q,t}\right)/2$ and $v_{\mathrm{hor},q,j,t} \to 1$; with the circumsolar term restored, the total then recovers Eq. (13). This limit is used as a consistency check on the angular integration (Section 3).

Reflected contributions. Sectors terminating on the ground carry the radiation reflected from it. Using the view factors of Eq. (6), the ground-reflected irradiance on element j is assembled in Section 2.1.3 as a sum over the visible segments of their radiosities, weighted by $\mathrm{VF}_{q_j \to g_i}$ and by the incidence-angle modifier appropriate to each viewing direction. Sectors in $\mathcal{M}_{\mathrm{nb}}$ carry the much weaker radiation reflected from the facing surface of the adjacent row,

$$I_{\mathrm{nb},q,j,t} = \sum_{m \in \mathcal{M}_{\mathrm{nb}}} \Delta CF_m\, \mathrm{IAM}(\theta_{q,j,m})\, J_{\mathrm{nb},m,t}, \tag{16}$$

where $J_{\mathrm{nb},m,t}$ is the radiosity of the module surface intercepted in sector m. This path is weak, because radiation reaching a module is largely absorbed rather than reflected, but it is retained because it is the physically correct destination for sectors that would otherwise be credited to the sky. The term $I_{\mathrm{grd},q,j,t}$ in Eq. (3) denotes the sum of both reflected contributions.

Obstruction therefore enters all three terms of Eq. (3), by the route appropriate to each. It enters the beam through the shadowed fraction $s_{q,j,t}$; it enters the sky term by restricting the summation to $\mathcal{M}_{\mathrm{sky}}$; and it enters the reflected term twice, once by restricting the module's view to the segments in $\mathcal{M}_i$, and once more through the reduced irradiance that the shaded and partly sky-obscured segments themselves receive, which is the subject of the next section.

2.1.3. Ground-reflected irradiance ($I_{\mathrm{grd},q,j,t}$) and ground albedo

The inter-row ground is divided into N_g segments of width Δx_i and centre x_i, with x measured from the ground projection of the lower module edge and running over one row pitch, $0 \le x \le p$. The front- and rear-facing ground arrays index the same periodic strip, so χ_i applies to both and the treated area is counted once.

Irradiance incident on a ground segment. A segment receives diffuse radiation through the portion of the sky it can see between the rows, and direct and circumsolar radiation only where it is not shadowed by a row:

$$G_{i,t} = I_{\mathrm{DHI},t}\,(1 - F_{1,t})\,\mathrm{VF}_{g_i\to\mathrm{sky}} + \left[u_{i,t} + (1-u_{i,t})\,\tau\right]\left(I_{\mathrm{cir},t} + I_{\mathrm{DNI},t}\cos\theta_{z,t}\right), \tag{17}$$

where $u_{i,t} \in [0,1]$ is the sunlit fraction of the segment and τ is the module transmission factor, which admits a small amount of radiation through the gaps between cells onto otherwise shaded ground. The Perez horizon-brightening term vanishes because the ground is horizontal. The sky view factor $\mathrm{VF}_{g_i\to\mathrm{sky}}$ depends only on geometry and is evaluated once; the sunlit fractions change with solar position and are recomputed each timestep, assigned fractionally at the two shadow boundaries so that the sunlit area varies continuously rather than in steps of one segment.

Local albedo and treatment coverage. The albedo of a segment is set by how much of it has been treated,

$$\rho_{i,t} = \rho_{\mathrm{base},i,t} + \chi_i\left(\rho_{\mathrm{treated},i,t} - \rho_{\mathrm{base},i,t}\right), \qquad \chi_i = \frac{\mathrm{length}\big([x_i^-, x_i^+] \cap \Omega\big)}{\Delta x_i}, \tag{18}$$

where Ω is the union of treated intervals across the row pitch and $\chi_i \in [0,1]$ is the treated fraction of segment i. Segments may therefore be fully treated, partially treated or untreated, and non-contiguous treatment strips require no change of formulation. Where Ω is specified by coordinates falling outside $[0,p]$, it is reduced modulo the pitch before the overlap in Eq. (18) is evaluated.

The fraction of the row pitch carrying treatment follows directly,

$$f_{\mathrm{cov}} = \frac{1}{p}\sum_{i=1}^{N_g}\chi_i \Delta x_i, \qquad 0 \le f_{\mathrm{cov}} \le 1, \tag{19}$$

and is the scalar varied in the coverage parametric study. Two treatments with equal f_{cov} but different Ω incur the same cost and deliver different rear irradiance, because segments differ in illumination and in view factor to the module.

Reflection and transfer to the module. Under a first-reflection Lambertian assumption the radiosity leaving segment i is

$$J_{i,t} = \rho_{i,t}\,G_{i,t}, \tag{20}$$

and the ground-reflected irradiance on element j of face q is the sum of the radiosities of the segments that element can see, weighted by the view factors of Eq. (6) and by the incidence-angle modifier appropriate to each viewing direction:

$$I_{\mathrm{grd},q,j,t} = \sum_{i=1}^{N_g} J_{i,t}\,\mathrm{VF}_{q_j\to g_i}\,\mathrm{IAM}_{q,j,i} \;+\; I_{\mathrm{nb},q,j,t}, \qquad q \in \{F,R\}, \tag{21}$$

with $I_{\mathrm{nb},q,j,t}$ the neighbouring-row term of Eq. (16). Because $\mathrm{VF}_{q_j\to g_i}$ is accumulated from the angular sectors that terminate on segment i, a segment hidden from an element by an intervening row contributes nothing to it, and the front and rear faces draw on different parts of the ground automatically.

Incremental irradiance from treatment. Subtracting the untreated case from Eq. (21) gives the irradiance attributable to the treatment,

$$\Delta I_{\mathrm{grd},q,j,t} = \sum_{i=1}^{N_g}\chi_i\left(\rho_{\mathrm{treated},i,t} - \rho_{\mathrm{base},i,t}\right)G_{i,t}\,\mathrm{VF}_{q_j\to g_i}\,\mathrm{IAM}_{q,j,i}, \tag{22}$$

in which the neighbouring-row term cancels because it is evaluated from the baseline ground in both cases.

Equation (22) shows that the value of treating a given segment is set by four coupled quantities: the local albedo increase, the irradiance the segment receives, its visibility from the module, and the optical transmission at the resulting incidence angle. A segment that is highly visible from the rear face contributes little if it lies in shadow for much of the year, and a strongly illuminated segment contributes little if neither face can see it. The spatial optimisation of Ω reported in Section 4 follows directly from this structure.

Linearity in the ground radiosity. The irradiance arriving at a ground segment does not depend on how reflective that segment is: $G_{i,t}$ in Eq. (17) is assembled from the sky and the direct beam alone. Albedo enters one step later, at Eq. (20). Equation (21) is therefore linear in the set of segment radiosities $\{\rho_{i,t}G_{i,t}\}$, and each segment contributes to the module independently of the albedo assigned to any other.

Two properties follow. First, the uniform-albedo case is the special case $\rho_{i,t} = \rho$, for which the sum collapses to ρ multiplying a view-factor-weighted mean of the segment irradiances. The spatially varying formulation is thus a generalisation of the reference formulation rather than a different model, and the verification reported in Section 3 applies to it unchanged. Second, at fixed χ_i the incremental irradiance of Eq. (22) is exactly proportional to $\rho_{\mathrm{treated}} - \rho_{\mathrm{base}}$, which the implementation asserts as a numerical self-test: doubling the albedo increment must double the computed irradiance gain.

This linearity is a consequence of the first-reflection assumption. Radiation that leaves the ground, strikes a module and returns to the ground is not tracked, and including it would introduce a term of order ρ^2 in $G_{i,t}$. Radiation reflected from the ground onto the facing surface of a neighbouring row and thence to the module is retained, and remains linear in the segment radiosities. The truncation follows the reference formulation [33] and is common to the baseline and treated cases, so it does not bias the paired comparison from which the treatment benefit is obtained.

2.1.4. Face averaging and effective bifacial irradiance

The area-averaged irradiance on face q is

$$\overline{I}_{q,t} = \frac{\sum_{j=1}^{N_q} A_{q,j} I_{q,j,t}}{\sum_{j=1}^{N_q} A_{q,j}}, \qquad q \in \{F, R\}, \tag{23}$$

and the irradiance available for conversion is

$$I_{\mathrm{eff},t} = f_{\mathrm{opt},F} f_{\mathrm{mis},F,t} \overline{I}_{F,t} + \varphi_{\mathrm{bif}} f_{\mathrm{opt},R} f_{\mathrm{mis},R,t} \overline{I}_{R,t}, \tag{24}$$

where φ_{bif} is the module bifaciality factor and f_{opt} and f_{mis} account for side-specific optical losses not already represented by the incidence-angle modifier and for electrical mismatch arising from irradiance non-uniformity. The bifaciality factor is applied only after the physical rear irradiance has been computed and does not alter it. Annual irradiation on each face and the effective annual bifacial irradiation follow as $H_q = \sum_t \overline{I}_{q,t}\Delta t$ and $H_{\mathrm{eff}} = \sum_t I_{\mathrm{eff},t}\Delta t$.

The treated ground area is taken from the same treatment definition used in the irradiance calculation,

$$A_{\mathrm{treated}} = L_{\mathrm{row,tot}} \sum_{i=1}^{N_g} \chi_i \Delta x_i, \tag{25}$$

with $L_{\mathrm{row,tot}}$ the cumulative modelled row length. This keeps the ground area responsible for the modelled irradiance gain identical to the area carrying the material, installation and maintenance costs of Section 2.3.

2.1.5. Treatment placement and coverage sweep

The treated set Ω enters the model through two independent degrees of freedom, and the parametric study varies them separately. The first is the coverage fraction f_{cov} of q. (19), which alone determines the treated area and therefore the cost. The second is the placement of Ω within the pitch at fixed coverage, which does not change the cost but does change the incremental irradiance, because Eq. (22) weights each segment by the product of its illumination $G_{i,t}$ and its visibility $\mathrm{VF}_{q_j \to g_i}$.

Placement is resolved by first evaluating, over the full meteorological year, the annual rear-side response $M_{R,i}$ of every ground segment to a unit increase in its own albedo. Because the rear irradiance is exactly linear in the segment radiosities and the treatment cost is uniform per unit area, the placement that maximises the incremental energy at any given coverage fraction is obtained by filling segments in descending order of $M_{R,i}$. The coverage sweep therefore steps f_{cov} over a discrete set spanning zero to full coverage, admitting segments in that order, and reports the optimal-placement envelope rather than one arbitrary strip layout. The resulting treated set is in general non-contiguous, which Eq. (18) accommodates without modification.

Since the cost is a function of f_{cov} alone while energy depends on both variables, the ratio of incremental energy to treatment cost is not constant across the sweep. That non-proportionality determines where the value-maximising coverage lies, and it is the quantity the results section reports.

Table 2: Irradiance-model settings for the reference case. Quantities marked calculated are evaluated at every timestep and are not replaced by annual-average values.

Symbol	Value	Description	Source
Site and meteorology			
ϕ, λ	$32.90°\mathrm{N}, 97.02°\mathrm{W}$	Dallas-Fort Worth International Airport; UTC-6, no daylight-saving correction applied to TMY timestamps.	[43, 44]
$N_t, \Delta t$	8760, 1 h	Hourly TMY3 record; solar position evaluated at the interval midpoint.	[43, 44]
$I_{\mathrm{DNI},t}, I_{\mathrm{DHI},t}$	Hourly series	Direct normal and diffuse horizontal irradiance driving the beam and Perez components.	[43]
Array geometry			
β_F, γ_F	$30°, 0°$	Fixed south-facing tilt; β_R and γ_R follow Eq. (1).	Present study
$L_m \times W_m$	2.382×1.134 m	Module slant length and width, portrait mounting.	[45]
GCR, p	0.35, 6.806 m	Ground-coverage ratio and resulting row pitch; varied in the sensitivity study.	Present study
C	1.00 m ($0.42\,L_m$)	Ground clearance of the lower module edge, quoted in metres and in slant lengths.	Present study
Discretisation			
N_q	20 per face	Module-face elements; grid independence verified in Section 3.	Present study
N_g	100 per pitch	Inter-row ground segments.	[33]
$N_\psi, \Delta\psi$	180, $1°$	Angular sectors per element over the outward hemisphere.	[33]
Optical and albedo inputs			
n_g	1.526	Cover refractive index in Eq. (8), applied to every angular sector.	[33]
τ	0.013	Module transmission factor for radiation reaching shaded ground between cells.	[33]
ρ_{base}	0.20	Natural ground albedo for maintained grass; replaced by a measured series where site data exist.	[46]
ρ_{treated}	0.70 (year 1)	Reflective treatment albedo; degradation imposed in the lifecycle model.	[16]
f_{cov}, Ω	0.50; value-ordered sweep	Treated fraction of the row pitch for the reference case, with segments admitted in descending order of annual rear-side response (Section 2.1.5).	Present study
φ_{bif}	0.80 ± 0.05	Rated rear-to-front maximum-power bifaciality.	[45]

2.2. Energy Yield Model

The energy-yield model converts the face irradiances of Section 2.1.4 into annual energy, once for the untreated baseline and once for the treated case. Both runs use the same weather file, geometry and loss assumptions, so that the difference between them isolates the effect of the ground treatment.

2.2.1. Cell Temperature and Thermal Losses

Module output is reduced by operating temperature above the $25°\mathrm{C}$ standard test condition (STC) reference. Cell temperature is estimated from the nominal operating cell temperature (NOCT) model [37],

$$T_{\mathrm{cell},t} = T_{\mathrm{amb},t} + (T_{\mathrm{NOCT}} - 20)\,\frac{I_{\mathrm{therm},t}}{800} \cdot \frac{9.5}{5.7 + 3.8\,v_t}\left(1 - \frac{\eta_{\mathrm{module}}}{0.9}\right), \tag{26}$$

where T_{NOCT} is the manufacturer-rated nominal operating cell temperature ($45°\mathrm{C}$ for the bifacial PERC modules considered here), v_t is the wind speed and η_{module} is the module electrical efficiency.

The driving irradiance in Eq. (26) is the total radiation absorbed by the module,

$$I_{\mathrm{therm},t} = \overline{I}_{F,t} + \overline{I}_{R,t}, \tag{27}$$

and not the effective irradiance $I_{\mathrm{eff},t}$ of Eq. (24). The bifaciality factor φ_{bif} describes the reduced *electrical* response of the rear cells; radiation incident on the rear face is absorbed and converted to heat in full. Applying φ_{bif} in the thermal model would therefore understate the cell temperature, and the error would grow with the rear contribution, which is precisely the quantity the ground treatment increases.

The temperature correction applied to module power is linear in cell temperature,

$$f_{\mathrm{temp},t} = 1 + \gamma_{P_{\mathrm{mp}}}\,(T_{\mathrm{cell},t} - 25), \tag{28}$$

where $\gamma_{P_{\mathrm{mp}}}$ is the module power temperature coefficient, typically $-0.35\%/°\mathrm{C}$ for bifacial PERC modules. Because $I_{\mathrm{therm},t}$ is higher in the treated case, the model self-consistently predicts a small rise in operating temperature under the ground treatment, which acts as a partial offset to the irradiance gain rather than being neglected.

2.2.2. Annual Energy Production

Annual energy production (AEP) follows the standard PV performance-model structure used in NREL PVWatts and comparable tools. Rated capacity is scaled by the ratio of effective plane-of-array irradiance to the STC reference irradiance, corrected for temperature, and reduced by a lumped system-loss term:

$$\mathrm{AEP} = \sum_{t=1}^{N_t} P_{\mathrm{rated}} \, \frac{I_{\mathrm{eff},t}}{I_{\mathrm{STC}}} \, f_{\mathrm{temp},t} \, (1 - L_{\mathrm{sys}}) \, \Delta t, \qquad I_{\mathrm{STC}} = 1000 \ \mathrm{W\,m^{-2}}. \tag{29}$$

Three points of bookkeeping matter here. The normalising irradiance is the STC reference at which P_{rated} is defined, not the site global horizontal irradiance. The summation runs over the hourly timesteps of the meteorological year, so that Eq. (29) returns an energy rather than a power. And L_{sys} covers only wiring, soiling, inverter conversion and availability losses; row shading is already represented by $s_{q,j,t}$ in Eq. (7) and electrical mismatch by $f_{\mathrm{mis},q,t}$ in Eq. (24), and including them again in L_{sys} would double-count them. P_{rated} is the front-side STC rating, the rear contribution having already been applied through φ_{bif} in $I_{\mathrm{eff},t}$.

Equation (29) is evaluated for the baseline and treated cases to give $\mathrm{AEP}_{\mathrm{base}}$ and $\mathrm{AEP}_{\mathrm{spray}}$, and the incremental first-year energy attributable to the treatment is

$$\Delta\mathrm{AEP}_{\mathrm{yr1}} = \mathrm{AEP}_{\mathrm{spray}} - \mathrm{AEP}_{\mathrm{base}}. \tag{30}$$

Specific yield, $\mathrm{AEP}/P_{\mathrm{rated}}$ in $\mathrm{kWh\,kWp^{-1}\,yr^{-1}}$, and capacity factor, $\mathrm{AEP}/\left(P_{\mathrm{rated}} \times 8760\right)$, are reported alongside AEP as cross-comparable performance benchmarks.

2.2.3. Multi-year Production Schedule

Two effects reduce the treated-case advantage over the project life. Module output degrades at an annual rate d, typically $0.5\%\,\mathrm{yr^{-1}}$ for modern crystalline-silicon modules, applied to both cases alike:

$$\mathrm{AEP}_{\mathrm{base},t} = \mathrm{AEP}_{\mathrm{base}} \, (1 - d)^{t-1}, \qquad t = 1, \ldots, n, \tag{31}$$

where n is the project lifetime in years. Separately, the reflectance of the ground treatment declines between reapplications, so the treated albedo $\rho_{\mathrm{treated},t}$ is itself a function of time.

Re-running the irradiance model for each year is unnecessary. Because $\Delta I_{\mathrm{grd},q,j,t}$ is exactly proportional to $\rho_{\mathrm{treated}} - \rho_{\mathrm{base}}$ at fixed treatment coverage (Section 2.1.3), the incremental energy scales by the same factor,

$$k_t = \frac{\rho_{\mathrm{treated},t} - \rho_{\mathrm{base}}}{\rho_{\mathrm{treated},1} - \rho_{\mathrm{base}}}, \qquad \Delta\mathrm{AEP}_t = \Delta\mathrm{AEP}_{\mathrm{yr1}} \, (1 - d)^{t-1} \, k_t, \tag{32}$$

with $k_1 = 1$ and k_t reset to unity at each reapplication year defined in Section 2.3. The treated-case schedule is then

$$\mathrm{AEP}_{\mathrm{spray},t} = \mathrm{AEP}_{\mathrm{base},t} + \Delta\mathrm{AEP}_t. \tag{33}$$

Equations (31) to (33) generate the multi-year energy schedule that drives the discounted cash-flow analysis, and they ensure that the reflectance decline assumed in the cost model is also reflected in the energy model rather than only in the reapplication expense.

2.3. Ground Treatment Cost Model

The area of ground requiring reflective treatment is derived from the plant capacity and layout rather than specified directly, and is taken from the same treatment definition used in the irradiance model. This keeps the ground area responsible for the modelled energy gain identical to the area carrying the material, installation and maintenance costs.

2.3.1. Plant Area and Treated Area

The total module area follows from rated capacity, the STC reference irradiance and module efficiency,

$$A_{\mathrm{panels}} = \frac{P_{\mathrm{rated}}}{I_{\mathrm{STC}} \, \eta_{\mathrm{module}}}, \qquad I_{\mathrm{STC}} = 1000 \ \mathrm{W\,m^{-2}}, \tag{34}$$

and the total farm area follows from the ground-coverage ratio, defined as the ratio of collector area to land area,

$$A_{\mathrm{farm}} = \frac{A_{\mathrm{panels}}}{\mathrm{GCR}}. \tag{35}$$

Normalising Eq. (35) by installed capacity gives the land-use intensity,

$$\mathrm{LUI} = \frac{A_{\mathrm{farm}}}{P_{\mathrm{rated}}}, \tag{36}$$

reported in $\mathrm{acres\,MW^{-1}}$ for cross-verification against installed plants [25] and against the optimal GCR choices characterised previously for different mounting configurations [7].

The treated area is not specified independently. It is the area of the segments carrying the elevated albedo in the irradiance model, so that the cost model and Eq. (25) refer to the same ground. Using the coverage fraction f_{cov} of Eq. (19), and noting that the modelled ground period spans the full pitch, the treated area is simply

$$A_{\mathrm{treated}} = f_{\mathrm{cov}}\, A_{\mathrm{farm}} = L_{\mathrm{row,tot}} \sum_{i=1}^{N_g} \chi_i \Delta x_i, \tag{37}$$

which reproduces Eq. (25) exactly.

Two features of this construction matter for the parametric study.

First, the treated region is not restricted to the open ground between rows. The ground beneath the module projection receives diffuse and transmitted radiation and is visible to the rear face at favourable angles, so it is a legitimate and in some geometries preferred target for treatment. Access roads, equipment pads and other permanently untreatable ground are represented by setting $\chi_i = 0$ over the corresponding intervals, rather than by a separate multiplicative factor, so that the exclusion is visible in the same geometry that drives the irradiance calculation.

Second, cost depends only on f_{cov}, whereas the energy gain depends on both f_{cov} and the placement of the treated set Ω, as set out in Section 2.1.5. Two treatments covering the same fraction of the pitch cost the same but deliver different rear irradiance, and the resulting non-proportionality between $\Delta\mathrm{AEP}$ and C_{spray} is what determines where the value-maximising coverage lies.

2.3.2. Treatment Cost, Degradation and Reapplication Economics

Upfront treatment capital expenditure is the treated area times the combined material and labour cost per unit area,

$$C_{\mathrm{spray}} = A_{\mathrm{treated}}\,(c_{\mathrm{material}} + c_{\mathrm{labour}})\,. \tag{38}$$

Reflective ground treatments are not permanent. Durability studies of comparable high-albedo ground materials report measurable reflectance decline over periods ranging from months to a few years, depending on material class, precipitation, soiling and mechanical wear [17, 13]. The treatment is therefore modelled as requiring periodic reapplication at a product-lifetime interval t_{reapp}, which restores the treated albedo to its year-one value.

The reflectance decline between reapplications is carried in the energy model through the factor k_t of Eq. (32), so the reflectance assumption appears in the energy and the cost calculations simultaneously rather than only as a recurring expense. Both require literature-supported inputs: the module degradation rate d, and the reflectance decay trajectory $\rho_{\mathrm{treated},t}$ for the specific material class. Where measured decay data are unavailable for the treatment considered, a linear decline between reapplications is assumed and the sensitivity of the results to that assumption is reported.

Over a project life of n years the number of reapplications is

$$N_{\mathrm{reapp}} = \left\lceil \frac{n}{t_{\mathrm{reapp}}} \right\rceil - 1, \tag{39}$$

and their combined present value is

$$\mathrm{PV}(C_{\mathrm{reapp}}) = C_{\mathrm{spray}} \sum_{k=1}^{N_{\mathrm{reapp}}} \frac{1}{(1+r)^{k\,t_{\mathrm{reapp}}}}. \tag{40}$$

Discounting only the first reapplication understates lifecycle cost materially: for $t_{\mathrm{reapp}} = 5$ yr, $n = 25$ yr and $r = 7\%$, the summation in Eq. (40) is 1.84 against 0.71 for a single term. The total lifecycle treatment cost in present-value terms is

$$\mathrm{PV}(C_{\mathrm{treatment,total}}) = C_{\mathrm{spray}} + \mathrm{PV}(C_{\mathrm{reapp}})\,. \tag{41}$$

2.3.3. Operating Cost Savings

A reflective ground treatment that suppresses vegetation displaces part of the recurring vegetation-management expense that the site would otherwise incur. This is a genuine benefit of the treatment and is accounted for here, alongside its costs, rather than being omitted or absorbed into the baseline operating expense. The avoided annual cost is

$$\Delta\mathrm{AOE}_t = A_{\mathrm{treated}}\, c_{\mathrm{veg}}\, \xi_t, \tag{42}$$

where c_{veg} is the annual vegetation-management cost per unit treated area at the site and $\xi_t \in [0, 1]$ is the fraction of that cost actually displaced in year t. The avoided vegetation-management credit carries a corresponding opportunity cost. Ground held under a reflective treatment is unavailable for vegetation-based co-use, including grazing, pollinator habitat and agrivoltaic cropping, and for solar thermal applications occupying the same area [47]. That cost is not monetised here.

The distinction between ξ_t and the optical decay factor k_t is worth preserving. Optical reflectance and vegetation suppression need not decline together: a treatment may lose solar-weighted reflectance to soiling while continuing to inhibit growth, or

conversely may be breached by vegetation before its reflectance has degraded. Tying the two to a single decay factor would impose a coupling that the durability literature does not support, so ξ_t is specified separately and its value stated with the treatment properties.

Equation (42) enters the analysis through the net annual cash flow of Section 2.4, where it is added to the incremental energy revenue. It is reported separately from the energy benefit, because a treatment whose economics depend principally on avoided mowing rather than on rear-side irradiance gain is a different proposition from one justified on energy yield, and the two should not be presented as a single undifferentiated return.

2.4. Financial Model

The financial model evaluates the ground treatment both as a modification to the whole plant and as a standalone capital investment. All quantities are drawn from the energy and cost models of Sections 2.2 and 2.3, so that the reflectance decay, the reapplication schedule and the avoided vegetation-management expense appear consistently in every metric. The financial and cost inputs for the reference case are collected in Table 3.

2.4.1. Levelised Annual Quantities

Energy and operating-cost streams vary from year to year: module output degrades, the treatment reflectance declines between reapplications, and the avoided vegetation cost need not follow either. Any annual series X_t is therefore reduced to its levelised equivalent,

$$\overline{X} = \frac{\displaystyle\sum_{t=1}^{n} X_t \,(1+r)^{-t}}{\displaystyle\sum_{t=1}^{n} (1+r)^{-t}}, \tag{43}$$

which is the constant annual value with the same present value as the series itself. Equation (43) is applied to $\mathrm{AEP}_{\mathrm{base},t}$, $\mathrm{AEP}_{\mathrm{spray},t}$, $\Delta\mathrm{AEP}_t$ and $\Delta\mathrm{AOE}_t$. Using first-year values in their place would overstate the energy available to service the investment: for module degradation alone at $d = 0.5\%\,\mathrm{yr}^{-1}$ with $n = 25$ and $r = 7\%$, the levelised energy is 4.4% below the first-year value, and the gap is considerably larger for the incremental energy because the treatment reflectance decays within each reapplication interval as well.

Table 3: Plant, treatment-cost and financial inputs for the reference case. Literature-supported values are cited. Values identified as present-study scenarios are modelling assumptions rather than empirical point estimates; absolute financial results are conditional on these assumptions.

Symbol	Value	Description	Source
Plant			
P_{rated}	$1\ \mathrm{MW_{dc}}$	Rated direct-current capacity. All extensive results scale linearly with this value; LCOE_{Δ}, IRR, relative energy gain and $\rho^{\min}$ are independent of it.	Present study
η_{module}	0.214	Module efficiency at STC, giving $3.30\ \mathrm{acres\,MW_{dc}^{-1}}$ at $\mathrm{GCR} = 0.35$.	[45]
DC/AC	1.30	Inverter loading ratio. Not enforced as a power limit in Eq. (29).	[48]
L_{sys}	0.15	Aggregate loss used by the simplified DC-energy model. Combining the PVWatts default loss categories while omitting its 3% generic shading term (row shading is modelled explicitly) and applying the separate 96% nominal inverter efficiency gives a 14.96% DC-to-AC loss, rounded to 15%.	[49]
$f_{\mathrm{opt},q}, f_{\mathrm{mis},q,t}$	1.0	Side-specific optical and mismatch factors of Eq. (24), set to unity; residual optical and mismatch losses are represented by L_{sys}.	Present study
d	$0.5\%\ \mathrm{yr^{-1}}$	Module degradation rate.	[48]
$\gamma_{P_{\mathrm{mp}}}, T_{\mathrm{NOCT}}$	$-0.35\%\ ^{\circ}\mathrm{C}^{-1}, 45^{\circ}\mathrm{C}$	Module power temperature coefficient and nominal operating cell temperature.	[45]
Ground treatment			
$c_{\mathrm{material}}, c_{\mathrm{labour}}$	$1.50, 0.75\ \mathrm{USD\,m^{-2}}$	Reference scenario, giving $2.25\ \mathrm{USD\,m^{-2}}$ installed. The material/labour split is not a supplier quotation. For comparison, Lewis et al. calculate a breakeven installed-cost range of 2.50–$4.60\ \mathrm{USD\,m^{-2}}$, rather than reporting an observed market cost.	Present-study scenario; [16]
$t_{\mathrm{reapp}}, N_{\mathrm{reapp}}$	5 yr, 4	Replacement interval for a polymeric white ground cover. The tested tarp was not expected to retain its integrity beyond five years, and its capital cost was modelled as recurring every five years. Four replacements follow from Eq. (39) for $n = 25$ yr.	[17, 50]
ρ_{end}	0.50	End-of-cycle scenario value. Field measurements document declining white-tarp reflectance during a nine-month campaign but do not establish an albedo of 0.50 after five years; this endpoint is therefore varied in the sensitivity analysis.	[17]; present-study scenario
c_{veg}, ξ_t	$0.05\ \mathrm{USD\,m^{-2}\,yr^{-1}}$, 0.80	The unit cost equals approximately $203\ \mathrm{USD\,acre^{-1}\,yr^{-1}}$, matching the reported median annual mowing cost for turfgrass at utility-scale PV sites. The 80% displaced fraction is a scenario assumption because published studies do not establish a generally applicable displacement percentage.	c_{veg}: [51]; ξ_t: present-study scenario
Finance			
r, n	7%, 25 yr	Discount rate (WACC) and project lifetime. The benchmark uses a 30 yr recovery period.	[48]
$P_{\mathrm{elec},1}, e$	$45\ \mathrm{USD\,MWh^{-1}}, 2\%\ \mathrm{yr^{-1}}$	Reference electricity price and nominal escalation convention. The price lies within the reported 40–80 $\mathrm{USD\,MWh^{-1}}$ range for post-2021 US solar PPAs outside CAISO and the non-ISO West. Those published prices are levelised contract values, so $45\ \mathrm{USD\,MWh^{-1}}$ is a scenario point rather than an observed first-year mean. The 2% rate is a general inflation convention, not an empirically measured PPA escalator.	[52, 53]; present-study scenario
$\mathrm{TCC_{base}}$	$1.10\ \mathrm{USD\,W_{dc}^{-1}}$	Total capital cost net of the investment tax credit. The benchmark $1.55\ \mathrm{USD\,W_{dc}^{-1}}$ for a fixed-tilt, ground-mounted commercial system with bifacial modules, reduced by a 30% credit, gives $1.09\ \mathrm{USD\,W_{dc}^{-1}}$.	[48]
AOE	$20\ \mathrm{USD\,kW_{dc}^{-1}\,yr^{-1}}$	Annual operating expense for the benchmark system, excluding the vegetation-management credit of Eq. (42).	[48]
ITC	Applied to $\mathrm{TCC_{base}}$ only	Treatment capital cost is not assumed to qualify; therefore, C_{spray} enters Eqs. (46) and (53) gross.	Present study
$r_{\mathrm{rein}}, r_{\mathrm{fin}}$	7%, 7%	Reinvestment and financing rates in Eq. (55), both set equal to the discount rate.	Present study

2.4.2. Capital Recovery Factor and Levelised Cost of Energy

Following standard NREL techno-economic methodology [38], upfront capital costs are converted to an equivalent uniform annual payment through the capital recovery factor

$$\mathrm{CRF} = \frac{r\,(1+r)^{n}}{(1+r)^{n}-1}, \tag{44}$$

where r is the discount rate, taken as the weighted average cost of capital (WACC). As $r \to 0$, $\mathrm{CRF} \to 1/n$, recovering the

straight-line amortisation case. The levelised cost of energy for the baseline case is

$$\mathrm{LCOE}_{\mathrm{base}} = \frac{\mathrm{TCC}_{\mathrm{base}} \cdot \mathrm{CRF} + \mathrm{AOE}}{\overline{\mathrm{AEP}}_{\mathrm{base}}}, \tag{45}$$

where $\mathrm{TCC}_{\mathrm{base}}$ is the total capital cost net of any applicable investment tax credit and AOE is the annual operating expense. This CRF-based formulation is the standard approach across utility-scale solar techno-economic analyses, from the original NREL specification [38] to current industrial benchmarking [54].

The treated-case LCOE adds the present-value lifecycle cost of the treatment, including all reapplications, to the total capital cost; uses the higher treated-case energy; and credits the avoided vegetation-management expense against the annual operating cost:

$$\mathrm{LCOE}_{\mathrm{spray}} = \frac{\left[\mathrm{TCC}_{\mathrm{base}} + \mathrm{PV}(C_{\mathrm{treatment,total}})\right] \mathrm{CRF} + \mathrm{AOE} - \overline{\Delta\mathrm{AOE}}}{\overline{\mathrm{AEP}}_{\mathrm{spray}}}. \tag{46}$$

Using $\mathrm{PV}(C_{\mathrm{treatment,total}})$ from Eq. (41) rather than the upfront cost alone is necessary for consistency with the incremental metric below; charging only the first application would understate the lifecycle burden of the treatment in the whole-plant metric while charging it in full in the standalone one. Whether the treatment cost itself qualifies for the investment tax credit applied to $\mathrm{TCC}_{\mathrm{base}}$ is stated explicitly with the financial inputs, because the assumption materially affects the result.

A negative value of $\mathrm{LCOE}_{\mathrm{spray}} - \mathrm{LCOE}_{\mathrm{base}}$ indicates that the treatment reduces the plant's levelised cost, implying that the additional energy it yields is worth more per dollar of capital deployed than the plant's existing generation.

The incremental LCOE isolates the treatment investment on its own terms by dividing its annualised net cost by the incremental energy it produces:

$$\mathrm{LCOE}_{\Delta} = \frac{\mathrm{PV}(C_{\mathrm{treatment,total}})\,\mathrm{CRF} - \overline{\Delta\mathrm{AOE}}}{\overline{\Delta\mathrm{AEP}}}. \tag{47}$$

LCOE_{Δ} is directly comparable to the contracted or wholesale electricity price: if it falls below that price, the treatment is economical on the value of the energy it adds, independently of its effect on whole-plant LCOE. Because the avoided vegetation-management expense enters the numerator, LCOE_{Δ} may be negative, which would indicate that the treatment is justified by operating-cost savings alone before any energy benefit is counted. That case is reported explicitly rather than being absorbed into a single figure, since it represents a different investment proposition from one justified on rear-side irradiance gain.

2.4.3. Break-even treated albedo

The linearity of Section 3.1 admits a closed-form design threshold that is more directly useful than the energy gain itself, because it converts a material specification into an economic one. Writing the first-year incremental energy as

$$\Delta\mathrm{AEP}_{\mathrm{yr1}} = \mathcal{K}(f_{\mathrm{cov}})\, SA_{\mathrm{treated}}\, (\rho_{\mathrm{treated}} - \rho_{\mathrm{base}}), \tag{48}$$

where $\mathcal{K}$ is the annual energy gain per unit treated area per unit albedo increment, and collecting the discounting of Eqs. (32) and (51) into

$$S = \sum_{t=1}^{n} \frac{(1-d)^{t-1}\, k_t\, P_{\mathrm{elec},t}}{(1+r)^{t}}, \tag{49}$$

the treatment net present value is linear in the albedo increment, and setting it to zero gives

$$\rho^{\min}_{\mathrm{treated}} = \rho_{\mathrm{base}} + \frac{(c_{\mathrm{material}} + c_{\mathrm{labour}}) \left[1 + \sum_{k=1}^{N_{\mathrm{reapp}}} (1+r)^{-k\, t_{\mathrm{reapp}}}\right] - c_{\mathrm{veg}} \sum_{t=1}^{n} \xi_t\, (1+r)^{-t}}{\kappa(f_{\mathrm{cov}})\, S}. \tag{50}$$

The treated area cancels, because both the cost and the energy gain are proportional to it. Equation (50) therefore expresses the minimum reflectance a product must deliver for the treatment to repay its cost, in terms of quantities a developer knows before selecting a supplier: the unit costs, the reapplication interval, the contract price and its escalation, the discount rate, and the avoided vegetation-management expense.

The threshold is not, however, independent of coverage. The response $\mathcal{K}$ is the mean per-unit-area response of the ground actually treated, and under the value-ordered filling of Section 4.2 that mean falls as coverage increases, because progressively less valuable ground is being added. A treatment applied narrowly alongside the rows therefore repays itself at a lower reflectance than the same product applied across the full pitch. At the reference unit cost and contract price, $\rho^{\min}$ is 0.36 at 10% coverage, 0.43 at 50% and 0.50 at full coverage. This is the slope of the zero contour in Figure 9(b), and it is the quantitative form of the procurement guidance in Section 4.5: reflectance and placement are substitutes, and a lower-reflectance product can still be economic if it is applied where the ground is worth most.

2.4.4. Net Present Value and Internal Rate of Return

The treatment is also evaluated as a standalone capital investment using discounted cash-flow analysis [39]. The net annual cash flow combines the incremental energy revenue, the avoided operating expense, and any reapplication outlay falling in that year:

$$\mathrm{CF}_t = \Delta\mathrm{AEP}_t\, P_{\mathrm{elec},t} + \Delta\mathrm{AOE}_t - C_{\mathrm{reapp},t}, \qquad P_{\mathrm{elec},t} = P_{\mathrm{elec},1}\,(1+e)^{t-1}, \tag{51}$$

where $\Delta\mathrm{AEP}_t$ follows from Eq. (32), $\Delta\mathrm{AOE}_t$ from Eq. (42), e is the assumed annual electricity-price escalation rate, and

$$C_{\mathrm{reapp},t} = \begin{cases} C_{\mathrm{spray}}, & t = k\,t_{\mathrm{reapp}}, \quad k = 1, \ldots, N_{\mathrm{reapp}}, \\ 0, & \text{otherwise.} \end{cases} \tag{52}$$

The net present value is then

$$\mathrm{NPV} = \sum_{t=1}^{n} \frac{\mathrm{CF}_t}{(1+r)^t} - C_{\mathrm{spray}}, \tag{53}$$

with the initial application treated as an outlay at $t = 0$. A positive NPV indicates that the treatment earns a return in excess of the discount-rate hurdle and creates economic value; a negative NPV indicates that it does not. The internal rate of return is the discount rate r^* at which Eq. (53) evaluates to zero,

$$0 = \sum_{t=1}^{n} \frac{\mathrm{CF}_t}{(1+r^*)^t} - C_{\mathrm{spray}}, \tag{54}$$

and the investment is accepted under the standard decision rule $r^* > \mathrm{WACC}$ [39].

Where the cash-flow series changes sign more than once within the project horizon, for example a large reapplication outlay following several years of positive net cash flow, Eq. (54) may admit multiple mathematically valid roots. The reapplication schedule of Eq. (52) makes this the expected case rather than an edge case. The modified internal rate of return resolves the ambiguity by specifying explicit financing and reinvestment rates,

$$\mathrm{MIRR} = \left[\frac{\displaystyle\sum_{t=1}^{n} \mathrm{CF}_t^{+}\,(1+r_{\mathrm{rein}})^{n-t}}{\displaystyle\sum_{t=0}^{n} \left|\mathrm{CF}_t^{-}\right|\,(1+r_{\mathrm{fin}})^{-t}} \right]^{1/n} - 1, \tag{55}$$

where CF_t^{+} and CF_t^{-} are the positive and negative cash flows, r_{rein} is the reinvestment rate, r_{fin} is the financing rate, and the initial outlay C_{spray} is included among the negative flows at $t = 0$. MIRR is reported alongside IRR wherever the sign of CF_t changes more than once.

2.4.5. Payback Period

Two complementary payback metrics are reported. Simple payback divides the upfront investment by the first-year incremental net benefit, neglecting the time value of money:

$$\mathrm{Payback}_{\mathrm{simple}} = \frac{C_{\mathrm{spray}}}{\Delta\mathrm{AEP}_{\mathrm{yr1}} P_{\mathrm{elec},1} + \Delta\mathrm{AOE}_1}, \tag{56}$$

where the denominator is the first-year cash flow of Eq. (51) excluding any reapplication outlay. Discounted payback instead identifies the first year t^* at which the cumulative discounted cash flow turns non-negative,

$$t^*: \quad \sum_{t=1}^{t^*} \frac{\mathrm{CF}_t}{(1+r)^t} \geq C_{\mathrm{spray}}, \tag{57}$$

which is more conservative than simple payback and, unlike simple payback, is consistent with the NPV decision rule.

Discounted payback can appear unusually long, or fail to occur within the analysis horizon at all, when a large reapplication outlay falls late in the project life and insufficient time remains to recover it through discounted cash flow, even where the overall NPV is strongly positive. This is a known characteristic of payback metrics applied to long-lived assets with a lumpy cost structure [39]. NPV and IRR, rather than discounted payback, are therefore treated as the primary decision metrics throughout the analysis, with payback reported for comparability with industry practice.

3. Model Verification and Validation

The model was evaluated at three levels, and the three are not interchangeable. *Verification* compares the implementation against a reference that shares its inputs and its stated physics, so the only admissible residual is rounding. *Validation* compares it against physical measurements, and its admissible residual is set by the measurement uncertainty and by the published performance of comparable models. *External benchmarking* compares derived quantities against fleet statistics; it bounds gross error but cannot verify, because the comparator systems differ in site, technology and financing. Table 4 classifies every case on this basis.

3.1. Implementation

The irradiance model is implemented by calling the view-factor, shading, sky-transposition and optical routines of the NREL `bifacialvf` reference code [33, 40] directly, rather than by reimplementing them. Agreement with the reference is therefore structural rather than approximate, and the reference's own validation history is inherited.

The single extension is the generalisation of the ground reflection to a spatially varying albedo. In the reference formulation the ground term enters as $\langle G \rangle_{\mathrm{fov}}\, \rho$, a length-weighted mean of segment irradiances inside each angular sector multiplied by a scalar albedo. That expression is linear in the array $\rho_i G_i$, so supplying the segment radiosities $J_{i,t} = \rho_{i,t} G_{i,t}$ of Eq. (20) in place of the segment irradiances, with the scalar albedo set to unity, evaluates $\langle \rho G \rangle_{\mathrm{fov}}$ exactly. No view factor, shading factor or optical correction is altered. Two consequences follow: the uniform-albedo case reproduces the reference identically, so the verification below is inherited by the spatially varying model; and the incremental irradiance is exactly proportional to$\rho_{\mathrm{treated}} - \rho_{\mathrm{base}}$, which the implementation asserts at run time as a numerical self-test.

3.2. Verification of the irradiance model

The model is verified against the fixed-tilt benchmark distributed with the reference implementation [33]: an interior row at Richmond, Virginia, for the hour ending 12:00 on 1 January, with $I_{\mathrm{DNI}} = 10$ and $I_{\mathrm{DHI}} = 126\ \mathrm{W\,m^{-2}}$, $\rho = 0.62$, $\beta_F = 10^\circ$, $C = 0.4$, $D = 0.5152$, $\tau = 0.013$, six elements per face and 100 ground segments.

Every element agrees with the published value to within $0.05\ \mathrm{W\,m^{-2}}$, which is below the precision at which the reference values are printed. The face means are 124.70 against $124.72\ \mathrm{W\,m^{-2}}$ on the front and 23.39 against $23.38\ \mathrm{W\,m^{-2}}$ on the rear, giving $nRMSE$ of 0.026% and 0.108%. The errors change sign across the elements, with $MBE = -0.014$ and $+0.010\ \mathrm{W\,m^{-2}}$ against $MAE = 0.029$ and 0.021, so no systematic bias remains. The solar position is reproduced as $\theta_z = 61.3636^\circ$ and $\theta_F = 51.5770^\circ$, the average ground irradiance as 42.64 against $42.6\ \mathrm{W\,m^{-2}}$, and the broadband plane-of-array values as 131.8 and $79.9\ \mathrm{W\,m^{-2}}$.

The acceptance criterion is that every element agrees within 0.5% with no systematic sign; the residuals satisfy it by an order of magnitude. The sign condition matters as much as the magnitude, because twelve errors of one sign would indicate an unresolved bias whereas twelve scattered about zero are consistent with rounding of the published values.

3.3. Field validation of bifacial gain

Physical accuracy is assessed against twelve months of monitoring data from the bifacial test facility at the Technical University of Denmark in Roskilde ($55.7^\circ\mathrm{N}$, $12.1^\circ\mathrm{E}$), reported by Riedel-Lyngskær et al. [17], which compared eight bifacial simulation tools against measured string-level DC power, front and rear plane-of-array irradiance and module temperature.

The fixed-tilt system comprises 88 bifacial PERC modules of $295\ \mathrm{W_p}$, two in portrait, giving $25.96\ \mathrm{kW_p}$ at 25° tilt facing south, with $7.6\ \mathrm{m}$ pitch, ground-coverage ratio 0.40 and a torque-tube height of $2.30\ \mathrm{m}$. On-site global, diffuse and direct irradiance and albedo were measured with spectrally flat class A instruments; monthly mean albedo is used, annually averaging 21.6%. The model is driven by the official hourly Scenario S6 weather file, with solar position evaluated at each interval midpoint.

Bifacial gain follows the source study's Equation (2),

$$BG\,[\%] = \frac{H_R}{H_F}\,\varphi_{\mathrm{bif}}\,(1 - B_{\mathrm{loss}}) \times 100, \tag{58}$$

with $\varphi_{\mathrm{bif}} = 0.67$ determined from indoor flash current-voltage measurements on the deployed modules and $B_{\mathrm{loss}} = 0.032$, comprising 0.025 for electrical mismatch induced by non-uniform rear illumination and 0.007 for structural shading of the module rear. Both values are taken from the source study and are not adjusted here. The distinction matters: the raw rear-to-front irradiation ratio is an optical quantity, and comparing it directly against the measured electrically weighted gain would inflate the apparent error by roughly half again.

The source study concludes that, outside the winter months, two-dimensional view-factor fixed-tilt simulations agree with measured monthly bifacial gain to within ± 1 percentage point. That figure is adopted here as the acceptance criterion in preference to a threshold chosen by the present authors. The comparison is restricted to March through October following the same bracket, because the array has a shade angle of 16° while the winter-solstice sun elevation peaks at 12°, so the rows are partially shaded at practically all times in December and January and negative bifacial gains were measured in November and December.

The annual front-irradiation-weighted bifacial gain is 6.288% against 6.252% from the measured curve, a difference of $+0.037$ percentage point. From March to October the mean absolute error is 0.392, the RMSE 0.517 and the maximum 1.077 percentage points, with seven of the eight months inside the ± 1 percentage point criterion. The exception is March, at $+1.077$ percentage points, which exceeds the criterion by less than the digitisation uncertainty of the reference curve. April carries a known contamination in the opposite direction: an exceptional pollen event in late April 2019 soiled the monofacial reference more than the bifacial array, and the source study estimates the measured April gain to be overstated by as much as 1.5 percentage points, which is consistent with the -0.733 percentage point residual obtained here.

The measured range stated in the source study, 4.3 to 7.3% from March to October, brackets the digitised series used here, 4.5 to 7.1%, corroborating the digitisation to approximately 0.2 percentage points.

This validates the rear-irradiance pathway, which is the pathway the ground treatment acts on, at one northern-European site over one year at a ground-coverage ratio of 0.40 and a measured albedo near 0.22. It does not establish accuracy at the elevated albedos central to this study.

3.4. Verification of the energy conversion

The irradiance benchmark does not exercise the energy model. Equation (29) is therefore verified against `pvlib` [55], an independent open-source implementation, on three Typical Meteorological Year sites spanning the US resource range. Both receive identical hourly weather and identical plane-of-array irradiance, so the comparison isolates the conversion step. Given the same cell temperature the two agree to $10^{-14}\%$, which is machine precision, so the entire remaining difference between the two chains is attributable to the cell-temperature sub-model.

That sub-model is not constrained by the verification above. Compared against the Faiman and Sandia open-rack models on the same three sites, the nominal operating cell temperature model returns 1.9% more annual energy than Faiman and 3.7% more than Sandia, consistently in sign and magnitude [56, 41]. It therefore sits at the optimistic end of established practice, and the difference is reported as a sub-model uncertainty rather than absorbed. This is consistent with the field study above, in which the one participating tool using the NOCT model is a visible outlier in modelled module temperature while the remainder use Faiman with measured coefficients.

The consequence is asymmetric. The same factor multiplies the baseline and treated runs, so it cancels almost entirely in the relative gain $\Delta\mathrm{AEP}/\mathrm{AEP}$. It does not cancel in the absolute incremental energy: a 4% shift in f_{temp} carries approximately 4% into $\Delta\mathrm{AEP}$ and hence into LCOE_{Δ}, NPV and payback, and that sensitivity is reported with the results.

3.5. Verification of the financial equation

Equation (45) is verified against Ayadi et al. [26], who report the fixed charge rate, the capital cost of every desert and configuration, the fixed operating cost, and the resulting levelised cost. Inverting the expression for the implied specific yield tests it on every case they state numerically, and all five are reproduced. On the one case for which the source states the specific yield explicitly, the forward calculation gives 0.03122 against a published $0.0316\ \mathrm{USD\,kWh^{-1}}$, a residual of -1.20%; the published values are given to three significant figures, so $\pm 0.16\%$ is the reading precision of the source.

Two scope limits apply. The specific yield is taken from the source rather than computed, so this verifies the financial equation given an external energy input and says nothing about the energy model. And the source states fixed operating cost without specifying its basis; the agreement above assumes a per-$\mathrm{kW_p}$ reading, whereas a per-$\mathrm{kW_{ac}}$ reading converted at the stated ratio would give -5.02%. The per-$\mathrm{kW_p}$ reading is adopted and stated.

3.6. External benchmark: land-use intensity

Bolinger and Bolinger [25] report median power densities of 0.35 and $0.24\ \mathrm{MW_{dc}}$ per acre for fixed-tilt and tracking plants, from 736 US plants commissioned between 2007 and 2019, corresponding to 2.8 and $4.2\ \mathrm{acres\,MW_{dc}^{-1}}$. Their reciprocals reproduce the published energy densities to within 2%, so the published pair is mutually consistent.

Equation (29) contains no inverter power limit, so the reported energy gains are not reduced by inverter clipping. Because the treatment adds rear-side irradiance preferentially around solar noon, when a plant with a direct-to-alternating-current ratio above unity is closest to its inverter limit, the modelled gains are upper bounds on what a real plant of the same geometry would realise. Quantifying the clipping loss requires an inverter model and is left to future work.

Equation (36) is an accounting identity, $\mathrm{LUI} = 1/(\eta_{\mathrm{module}}\,\mathrm{GCR})$, in which the ground-coverage ratio is a design choice rather than a model output, so a single point value carries no information about model skill. The comparison is therefore reported as a bound: over module efficiencies of 0.18 to 0.214 and ground-coverage ratios of 0.30 to 0.45, six of the eight combinations fall inside the published band, and the reference case of Table 2 gives $3.30\ \mathrm{acres\,MW_{dc}^{-1}}$ at $\mathrm{GCR} = 0.35$. Because the published areas are whole-plant polygons including roads and setbacks, the implied packing fractions are lower bounds on the array ground-coverage ratio.

Table 4: Verification, field validation and external benchmarking of the present model. Percentage-point (pp) errors are used for bifacial gain.

Quantity	Comparator	Published	Present model and statistic	Class
Front irradiance	Marion et al. [33]	$124.72\ \mathrm{W\,m^{-2}}$	$124.70\ \mathrm{W\,m^{-2}}$; $nRMSE = 0.026\%$	Verification
Rear irradiance	Marion et al. [33]	$23.38\ \mathrm{W\,m^{-2}}$	$23.39\ \mathrm{W\,m^{-2}}$; $nRMSE = 0.108\%$	Verification
Bifacial gain	Roskilde field [17]	6.252% annual	6.288%; $+0.037$ pp annual, Mar-Oct $MAE = 0.392$ pp, max 1.077 pp, 7 of 8 months within ± 1 pp	Field validation
Energy conversion	`pvlib` [55]	`pvwatts_dc`	Identical to $10^{-14}\%$ at equal cell temperature	Verification
Cell temperature	Faiman, SAPM [55]	-	NOCT $+1.9\%$ and $+3.7\%$; reported as uncertainty	Sub-model bound
Levelised cost	Ayadi et al. [26]	$0.0316\ \mathrm{USD\,kWh^{-1}}$	0.03122; -1.20%; 5 of 5 published cases reproduced	Verification
Land-use intensity	Bolinger [25]	2.8-$4.2\ \mathrm{acres\,MW_{dc}^{-1}}$	3.30 at the reference $\mathrm{GCR} = 0.35$	External bound
Annual energy	Roskilde measured total	Not tabulated	Model reports $\pm 3.5\%$ envelope only; not scored	Not claimed

3.7. Limitations

The ground is treated as a Lambertian reflector truncated at the first reflection, so highly specular treatments and wet surfaces are outside the scope of the approximation and the neglected ground-to-module-to-ground path introduces a term of order ρ^2 that grows with treated albedo. The rows are effectively infinite and periodic, so edge rows and finite-row end effects are not represented, and structural obstruction from torque tubes and posts is neglected; the source study attributes its own winter fixed-tilt discrepancy to exactly such a feature.

The irradiance benchmark exercises a single sky condition, strongly diffuse and at low solar elevation, which tests the isotropic and ground-reflected pathways more severely than the beam and circumsolar pathways. The field validation covers one site, one year, one row geometry and a measured albedo near 0.22; no field dataset with a spatially varying ground treatment is known to the authors, so the partial-treatment extension remains a model-based extrapolation supported by the exactness argument of Section 3.1 rather than by measurement.

Annual energy has not been validated against a measured total: the source study reports modelling errors rather than the measured annual figure, so its $\pm 3.5\%$ envelope can be cited as a criterion but not scored against. Finally, the reflectance decay trajectory $\rho_{\mathrm{treated},t}$ and the vegetation-suppression factor ξ_t are inputs rather than model outputs, and the durability literature does not yet support either with the specificity the lifecycle analysis assumes; results are reported with an explicit sensitivity to both.

4. Results and Discussion

Results are reported for the reference plant of Table 2 using the verified model of Section 3. The baseline and treated cases share the same weather file, geometry and loss assumptions, so every difference reported below is attributable to the ground treatment alone.

Throughout, coverage sweeps fill ground segments in descending order of their annual rear-side response. Because the rear irradiance is exactly linear in the segment albedos (Section 3.1) and the treatment cost is uniform per unit area, this ordering is the optimal placement at every coverage fraction. The results below are therefore the optimal-placement envelope rather than one arbitrary strip layout.

4.1. Baseline plant

Figure 5 maps the unsubsidised levelised cost of the untreated plant over tilt and ground-coverage ratio. The optimum is interior in tilt and lies at the lower edge of the swept range in ground-coverage ratio: increasing the coverage ratio raises energy per unit land or the LUI, but increases inter-row shading too, which in turn reduces the ground area available to reflect onto the rear face. The tradeoff between GCR and LUI is well known [57, 58]. But this highlights that for partial round treatemnt, there is an additional tradeoff between the GCR and the LCOE because the GCR must be low to have room between the rows to apply reflective material.

Increasing solar panel tilt raises winter yield but deepens the row shadow. The lowest levelised cost in the swept domain, $66.3\ \mathrm{USD\,MWh^{-1}}$, occurs at a tilt of 30° and the smallest ground-coverage ratio considered, 0.25. Because the ground-coverage optimum sits on the boundary rather than in the interior, the reference case retains $\mathrm{GCR} = 0.35$, which is representative of deployed fixed-tilt plants [25], gives a levelised cost of $67.1\ \mathrm{USD\,MWh^{-1}}$, and leaves the treated-versus-untreated comparison unaffected. At that geometry the untreated plant produces $1.70\ \mathrm{GWh\,yr^{-1}}$, a specific yield of $1702\ \mathrm{kWh\,kWp^{-1}\,yr^{-1}}$ and a capacity factor of 19.4%, with a bifacial gain of 7.2% over the natural ground albedo.

Because $\mathrm{TCC_{base}}$ and AOE enter Eq. (45) identically at every point of the swept domain, they set the level of Figure 5 but not the location of its minimum, which is fixed by the energy model alone.

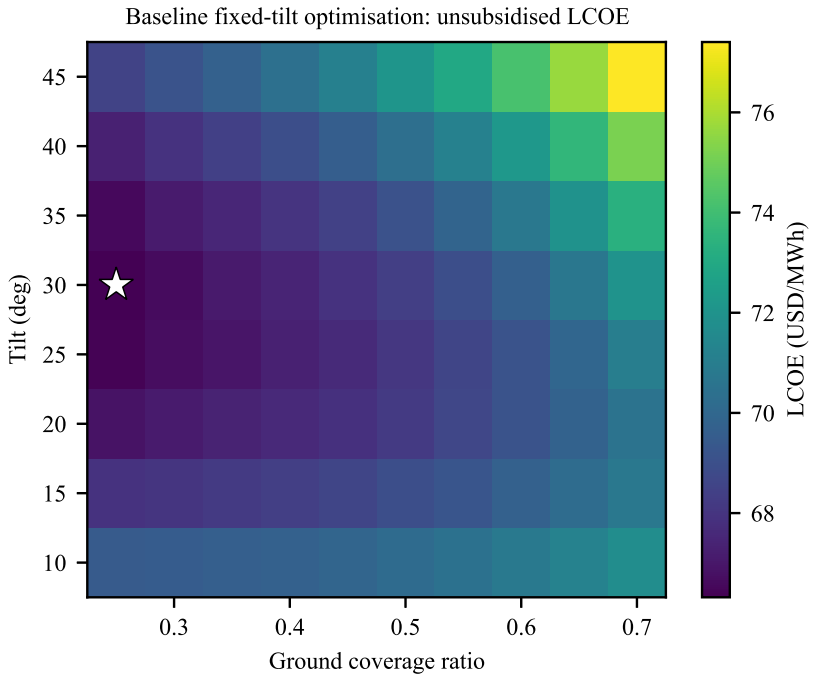


Figure 5: Unsubsidised levelised cost of the untreated bifacial plant over tilt and ground-coverage ratio. The star marks the optimum used as the baseline throughout.

4.2. Best location to apply ground treatment on

The value of treating a given ground segment is set by Eq. (22), as the product of the local albedo increase, the irradiance that segment receives over the year, its view factor to the module, and the optical transmission at the resulting incidence angle. The second and third of these vary strongly across the inter-row strip, so the ground is not uniformly worth treating. Figure 6 resolves that variation for the reference geometry.

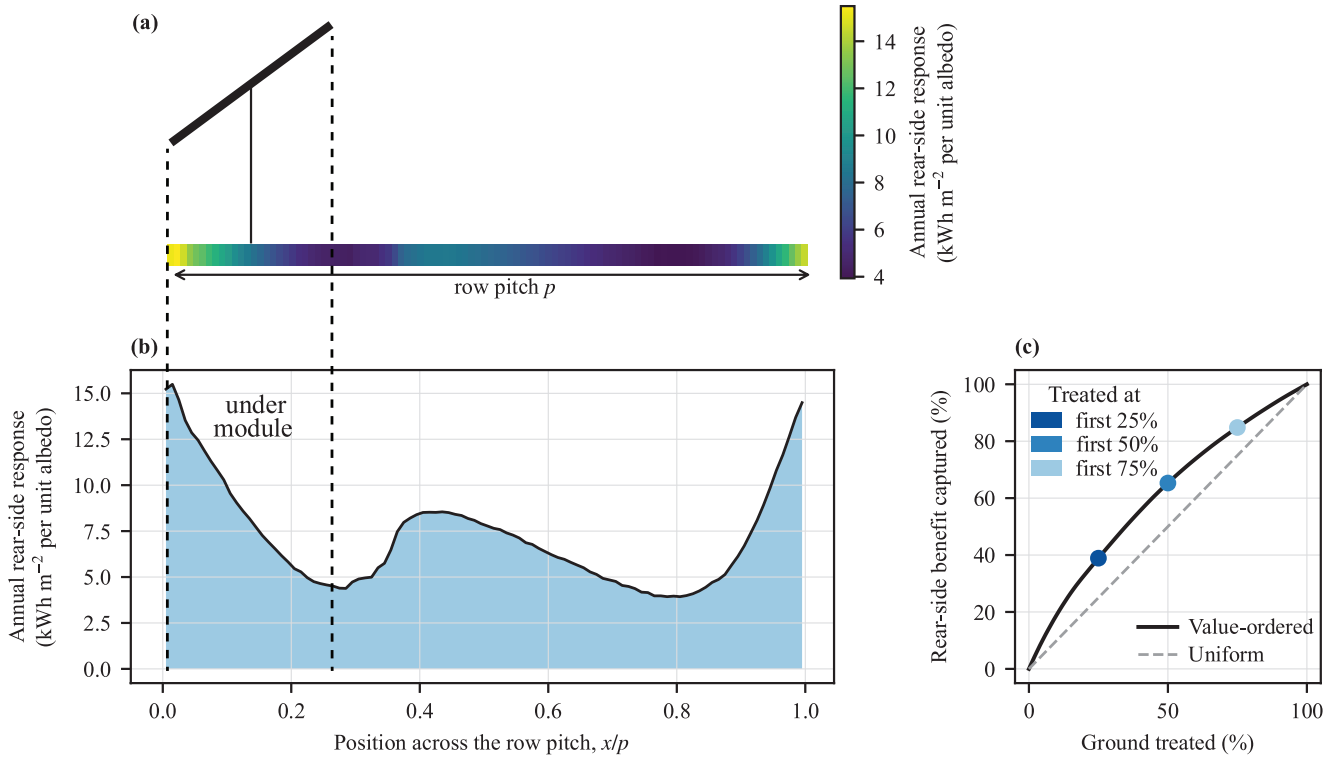


Figure 6: (a) Row cross-section with the inter-row ground shaded by its annual rear-side response, the change in annual rear irradiation per unit change in that segment's albedo. (b) The same quantity as a profile across the row pitch, with the segments selected at 25%, 50% and 75% coverage shaded in value order; the pale band marks the ground beneath the module projection. (c) Fraction of the total available rear-side benefit captured against fraction of ground treated, for value-ordered and uniform coverage.

Panel (a) shows that the response is concentrated near the module, and panel (b) that it falls away with distance across the pitch. The response peaks immediately beneath the row edge at 15.5 kWh m^{-2} per unit albedo, 2.2 times the pitch-averaged value, and falls to 3.9 kWh m^{-2} at $x/p \approx 0.8$, a variation of a factor of 3.9 across the pitch. The ground beneath the module projection is 30% of the pitch and carries 35% of the total benefit. Two mechanisms combine to produce this. The rear face subtends a larger solid angle at ground close to it, so the view factor is largest there; and the same ground is partially shaded from the direct beam for part of the day, so its irradiance is lower, which acts in the opposite direction. The observed profile is the net result, and it is not obtainable from either consideration alone.

Panel (c) is the consequence for design. Treating the ground in descending order of response captures a disproportionate share of the available benefit early: 39% of the total benefit is obtained from the first quarter of the area and 65% from the first half, against 25% and 50% for uniform coverage. Uniform treatment, by contrast, captures benefit in proportion to area, which is the diagonal. The gap between the two curves at a given coverage is the benefit forgone by treating the wrong ground, at identical cost.

This is the basis of the fill order used in every coverage sweep that follows. Because the rear irradiance is exactly linear in the segment albedos (Section 3.1) and the treatment cost is uniform per unit area, treating segments in descending order of response is the optimal placement at every coverage fraction, and the concavity of panel (c) carries directly into the energy and value curves of Section 4.4. A treatment specified only as a fraction of the ground, without reference to placement, therefore under-delivers against what the same expenditure could achieve.

The practical implication is that the treated region should be specified as a band adjacent to the rows rather than as a fraction of the site. This is also the more convenient specification operationally, since a band along the row is what an application vehicle can follow, and it leaves the mid-pitch ground, which is where access roads and equipment pads are usually placed, untreated.

4.3. Physical envelope of the achievable gain

Before the economics are considered it is useful to establish what the treatment can deliver at best, because the answer bounds every claim that follows. Figure 7(a) shows the annual energy gain against treated ground fraction for a family of treated albedos up to unity, evaluated at a bifaciality factor of 0.90, above the rated value of the modules considered here. Figure 7(b) shows the same quantity at full coverage and unit albedo as a function of the direct-to-alternating current ratio.

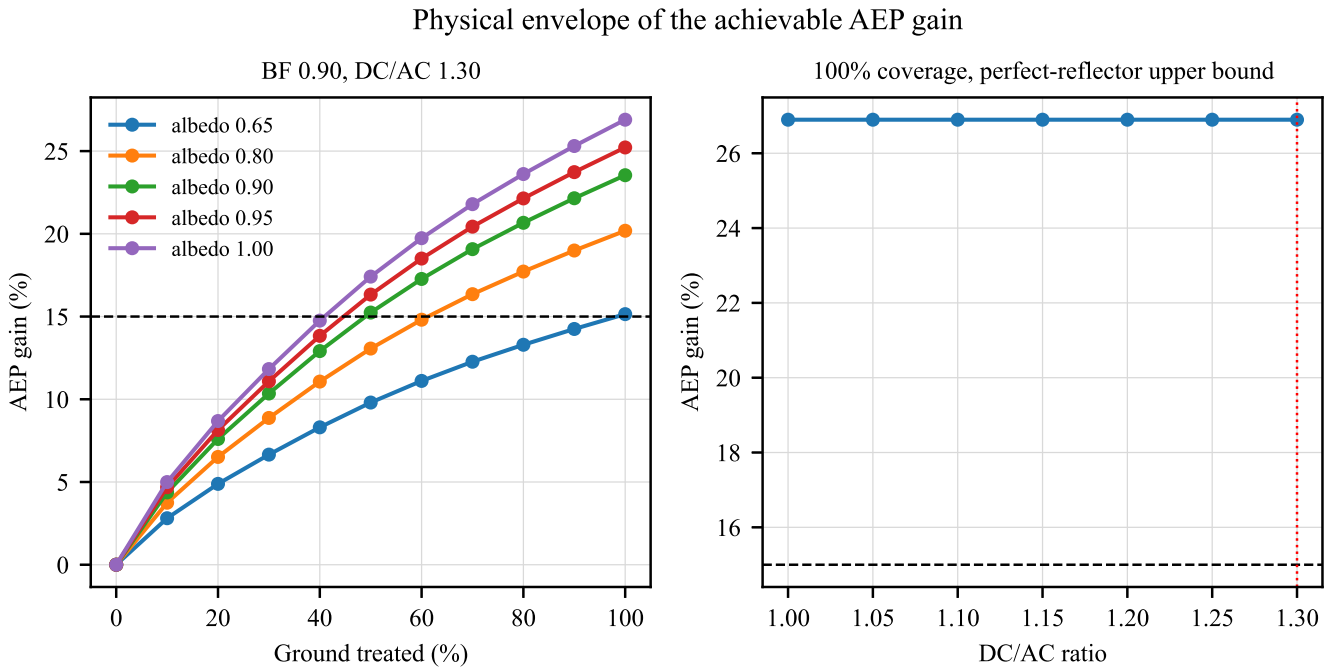


Figure 7: (a) Annual energy gain against treated ground fraction for treated albedos up to a perfect reflector, at a bifaciality factor of 0.90. (b) Gain at full coverage and unit albedo against direct-to-alternating current ratio; the dotted line marks the ratio of the reference plant.

The first and binding limit is optical: even a perfect reflector covering the entire inter-row ground can only increase the AEP so much, because only the fraction of the reflected hemisphere that the rear face can see contributes, and that fraction is fixed by the row geometry. That ceiling is 26.9% for the reference geometry at a bifaciality factor of 0.90, against 20.2% for a treatment of albedo 0.80 and 15.1% for albedo 0.65 at the same coverage. A second, electrical limit would be expected to act in the same direction, because the treatment adds irradiance preferentially at midday when the inverter is closest to its limit. Equation (29) contains no inverter power limit, however, so the modelled gain is independent of the direct-to-alternating current ratio and Figure 7(b) is flat across the range 1.00 to 1.30. The values reported here are therefore upper bounds for a plant with a finite inverter rating, and quantifying the clipping loss is left to future work (Section 3.7).

The practical limitation is that a target AEP expressed purely as a quantity of product applied cannot be met beyond this envelope, whatever the coverage. Increasing the treated albedo is more effective than increasing the treated area once the high-response ground has been covered. So treating more ground has diminishing returns. Increasing the albedo does not.

4.4. Treated ground fraction

Figure 8 shows the effect of treated ground fraction at the reference treated albedo. As seen in Figure 8(a), the energy gain is concave. The first increments of treatment are applied to the ground that the rear face sees most strongly and that receives the most irradiance, and each further increment is applied to progressively less valuable ground. The gain rises by 2.81 percentage points over the first tenth of the area but only 0.90 over the last tenth, a ratio of 3.1 between the first and last decile.

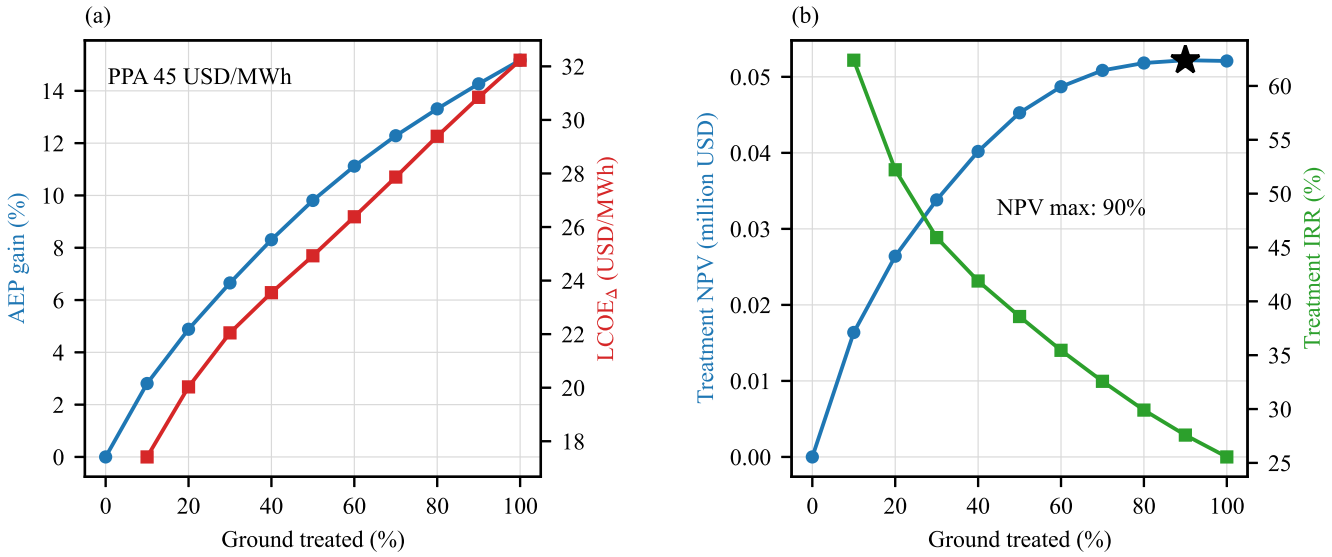


Figure 8: Effect of treated ground fraction at the reference treated albedo. (a) Annual energy gain and incremental levelised cost. (b) Treatment net present value and internal rate of return; the star marks the value-maximising coverage.

The cost of treatment is by contrast strictly proportional to the treated area, so the incremental levelised cost of the treatment rises monotonically with coverage, from 17.4 to 32.2 USD MWh^{-1} between one tenth and full coverage (Figure 8a). Each further increment of ground therefore delivers energy at a higher unit cost than the one before it, and the internal rate of return falls monotonically, from 62.4% at one tenth coverage to 25.6% at full coverage (Figure 8b).

Whether this produces an interior optimum depends on the cost of the treatment relative to the value of the energy it adds. Concavity of the benefit and linearity of the cost are not sufficient on their own; an interior optimum requires the marginal benefit to fall below the marginal cost somewhere inside the coverage range. At the reference unit cost of 2.25 USD m^{-2} and contract price of 45 USD MWh^{-1} the last increment of ground still very nearly repays itself, because the break-even reflectance at full coverage, 0.50, remains below the treated albedo of 0.70. Net present value is consequently flat above roughly 80% coverage, reaching 0.052 million USD at the plotted maximum of 90%, within 0.2% of its full-coverage value, where the annual energy gain is 14.3% at an incremental levelised cost of 30.8 USD MWh^{-1} and an internal rate of return of 27.6%. A well-separated interior optimum emerges only once the unit cost rises far enough that $\rho^{\min}$ at full coverage exceeds the available product reflectance: at 3.00 USD m^{-2} the value-maximising coverage falls to 58% of the pitch, where net present value stands 34% above its full-coverage value. The value-maximising coverage is therefore governed by the ratio of unit cost to contract price rather than by the shape of the response profile alone: the profile fixes *where* the material should go, and the cost-to-price ratio fixes *how much* of it.

The placement result, by contrast, follows directly from the structure of Eq. (22) and does not depend on the cost assumptions: the value of treating a given ground segment is the product of the local albedo increase, the irradiance that segment receives, its view factor to the module, and the optical transmission at the resulting incidence angle. Because the second and third factors vary strongly across the inter-row strip, the value of ground is not uniform, and a treatment specified as a fraction of the ground without regard to placement forgoes part of the available benefit at the same cost. The distinction matters commercially: at fixed coverage the two layouts at the extremes of the achievable range cost the same and deliver measurably different energy.

Field observations are consistent with this spatial structure. Bifacial modules positioned at the end of a row have been measured to produce a higher gain than otherwise identical modules in the row interior, because more of the reflecting ground is visible to them [59], which is the same view-factor mechanism operating at the array scale rather than within one inter-row strip.

4.5. Treated albedo

Figure 9 shows the effect of the treated albedo at fixed coverage, together with the joint response of net present value to coverage and albedo. The energy gain is linear in the treated albedo, which is a direct consequence of the linearity established in Section 3.1 i.e., the incident ground irradiance does not depend on the reflectance of the ground, so the reflected flux and hence the rear-side contribution scale in proportion to it.

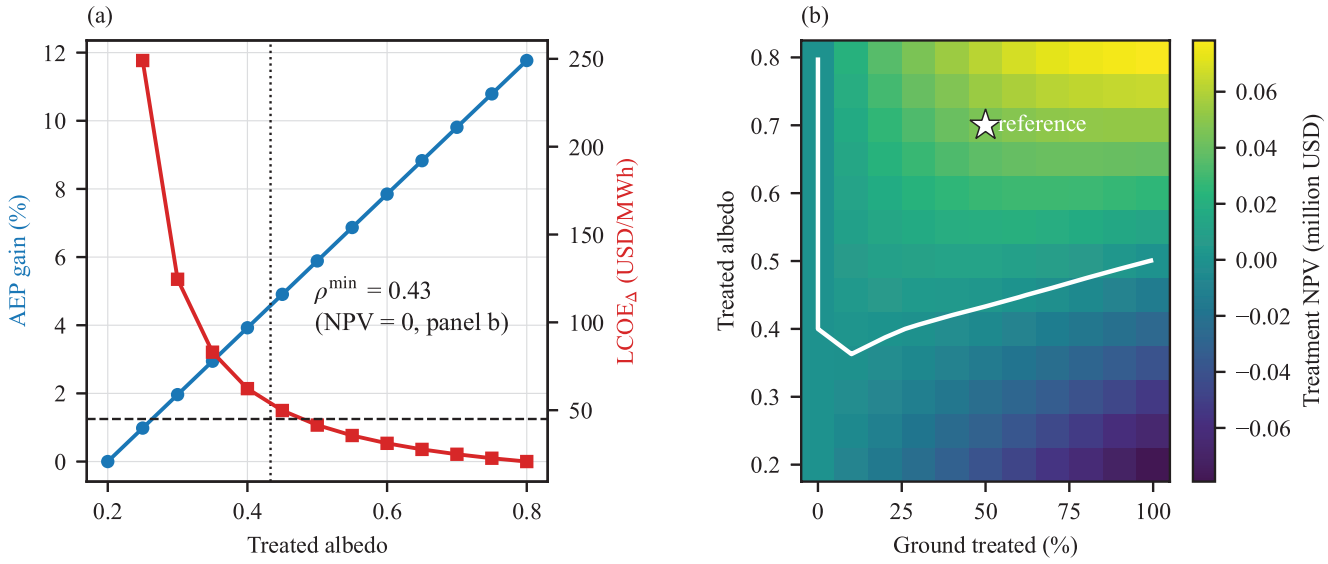


Figure 9: (a) Annual energy gain and incremental levelised cost against treated albedo at fixed coverage; the dotted line marks the albedo at which the treatment net present value changes sign. (b) Treatment net present value over treated ground fraction and treated albedo, with the zero contour in white and the reference case starred.

This linearity is supported by the literature. Alam et al. [15] reported that bifacial energy gain increases linearly with ground albedo across concrete, soil, white tile and white pebble surfaces at a fixed installation, and Riedel et al. [17] obtained the same proportionality from monitored data at Roskilde. Larger simulation studies reach the same conclusion: the annual plane-of-array irradiance gain has been shown to depend linearly on albedo, with the slope of that relationship reported as the appropriate quantity for predicting the effect of an arbitrary albedo change [8]. The present model reproduces this behaviour without it having been imposed, since it emerges from the radiative transfer rather than from a fitted relationship.

The magnitude is also consistent with reported values. For single-axis tracking systems, albedo conditions of 0.16 and 0.56 have been reported to give bifacial gains of 4% and 9% respectively [60], a slope of approximately 12 percentage points per unit albedo. Measured annual rear-irradiance gains span 5-10% for soil, above 20% for concrete and above 30% for white pebbles and white tiles [15], and tropical field measurements give bifacial gains of 8.7-16.5% depending on the ground material applied [59]. The present model gives 19.6 percentage points of annual energy gain per unit increase in treated albedo at the reference coverage, rising to 30.3 at full coverage. These slopes are not directly comparable with the tracked-system figure above, because they refer to a fixed-tilt geometry, to a treated fraction of the pitch rather than the whole ground, and to annual energy rather than rear-side irradiance; the agreement that matters here is the functional form rather than the coefficient.

The break-even albedo below which the treatment does not repay its cost is a more useful design quantity than the gain itself, because it converts a material specification into an economic threshold that a supplier can be held to. At the reference coverage and unit cost that threshold is 0.43, so the specified product albedo of 0.70 carries a margin of 0.27 against the reflectance decay assumed over the reapplication interval. Because the relationship is linear, this threshold scales predictably with the product and application cost and with the contract price, which is exploited in Section 4.7.

Panel (b) shows that the zero contour is much more sensitive to albedo than to coverage. A high-reflectance treatment applied to a modest fraction of the ground is economically preferable to a low-reflectance treatment applied broadly, at equal total cost. This has a direct procurement implication: specifying the reflectance of the product is more consequential than specifying the area to be covered.

4.6. Break-even treated albedo

Equation (50) gives the minimum reflectance at which the treatment repays its cost. Figure 10 evaluates it for the reference plant: (a) against treated ground fraction for a family of unit costs, and (b) against contract price at three coverages.

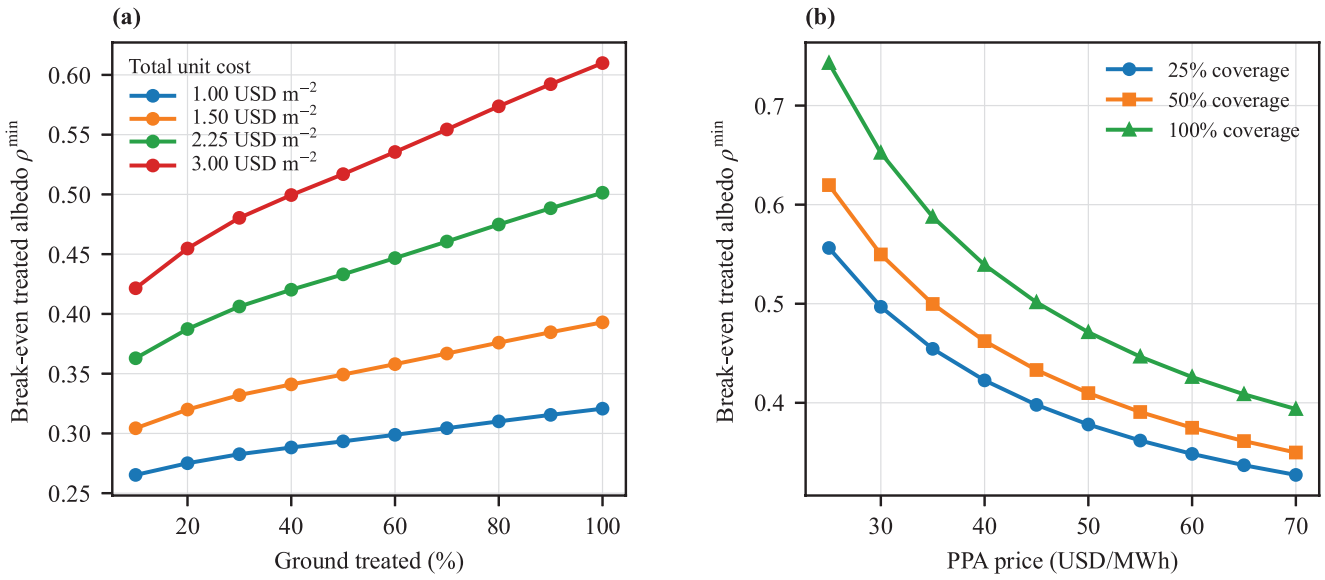


Figure 10: Break-even treated albedo, ($\rho^{\min}$), at which the ground treatment has zero net present value under the reference lifecycle assumptions. (a) Dependence on the fraction of ground treated for total installed unit costs of 1.00-3.00 USD,m^{-2}. (b) Dependence on the power-purchase-agreement (PPA) price at treated-ground coverages of 25%, 50%, and 100%, using the reference installed cost of 2.25 USD,m^{-2}. A treatment is economically viable when its delivered albedo equals or exceeds ($\rho^{\min}$).

4.7. Sensitivity to economic and module parameters

Figure 11 reports the sensitivity of the treatment case to the four parameters that the analysis is most exposed to.

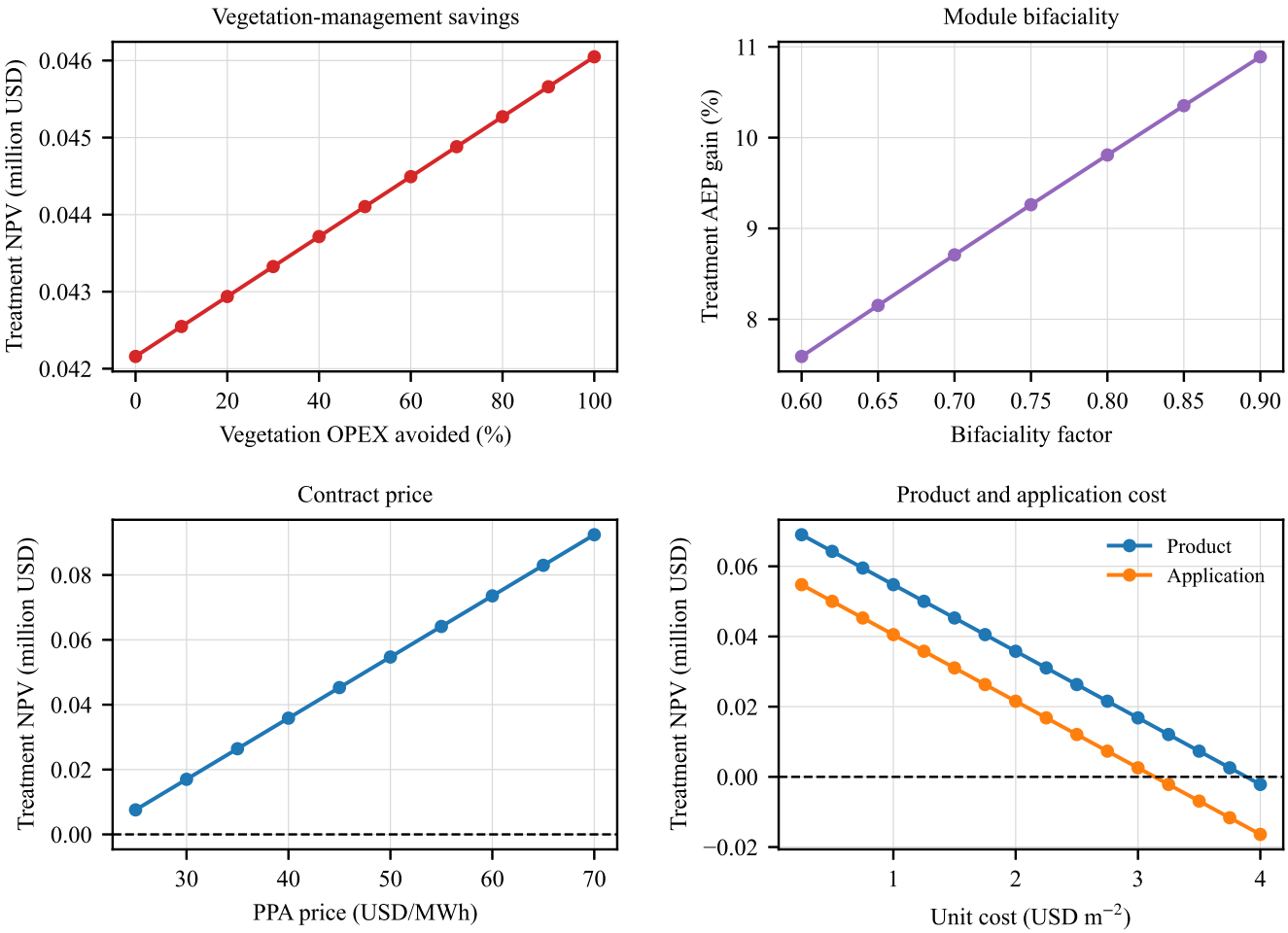


Figure 11: Sensitivity of the treatment case at the reference layout to vegetation-management savings, module bifaciality, contract price, and the product and application unit costs.

The avoided vegetation-management expense enters the net present value linearly and, at the upper end of the range considered, is a material fraction of the total return. Net present value rises from 0.042 to 0.046 million USD between no displacement of the mowing expense and complete displacement, so avoided vegetation management accounts for 8.4% of the total at full avoidance. The case for treatment therefore rests partly on a benefit that is not an energy benefit at all, and the two are reported separately here for that reason: a treatment justified principally by avoided mowing is a different commercial proposition, with different durability requirements, from one justified by rear-side irradiance gain.

The energy gain increases with module bifaciality, as expected, since the bifaciality factor multiplies the rear-side contribution that the treatment augments. The gain rises from 7.6% at $\varphi_{\mathrm{bif}} = 0.60$ to 10.9% at 0.90, or 1.1 percentage points of gain per 0.1 of bifaciality. Current commercial modules are moving in a favourable direction in this respect, with tunnel-oxide passivated-contact and heterojunction devices carrying higher bifaciality than the passivated-emitter-and-rear-contact technology they are displacing [60], so the value of ground treatment can be expected to rise with module technology independently of any change in the treatment itself.

Contract price and unit cost act in opposition and are close to linear over the ranges considered, so the treatment case can be summarised by the ratio of the two. Net present value crosses zero at a contract price of 21 USD MWh^{-1} at the reference unit cost, and at a combined product-and-application cost of 4.64 USD m^{-2} at the reference contract price. Product and application costs are reported separately because they are independently negotiable and because application cost scales differently with coverage: a single pass over a larger area is cheaper per unit area than several passes over a smaller one.

4.8. Cash flow and lifecycle behaviour

Figure 12 shows the incremental cash flow of the treatment against the untreated baseline. Plotting the difference rather than the two plant-level cash flows is necessary because the treatment is a small perturbation on a large project, and the reapplication outlays would otherwise not be distinguishable.

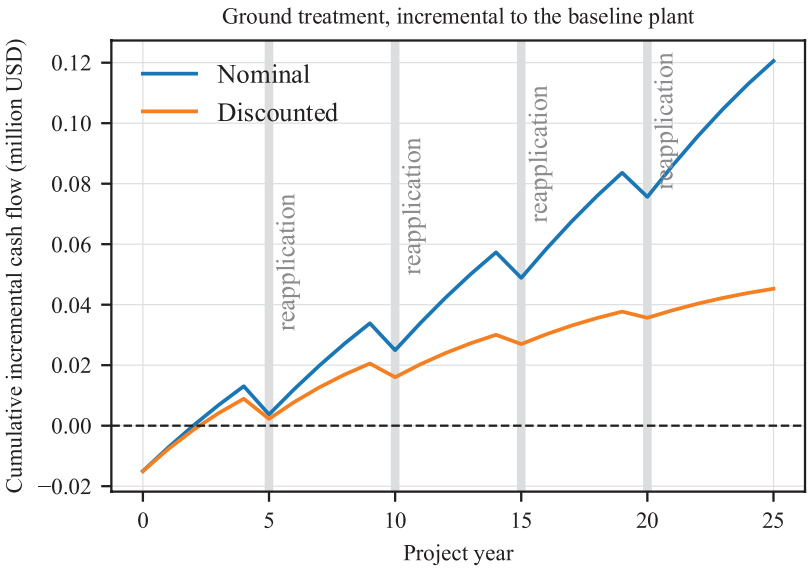


Figure 12: Cumulative incremental cash flow of the ground treatment against the untreated baseline, in nominal and discounted terms. Steps mark reapplication years.

Two features govern the lifecycle behaviour. The first is the reapplication schedule, which imposes a step outlay at each product-lifetime interval and is the reason the discounted and nominal curves diverge as the project matures. The second is the decline in treated reflectance between reapplications, which reduces the incremental energy within each interval and is carried in the energy model through Eq. (32) rather than being applied only as a recurring expense. With $t_{\mathrm{reapp}} = 5$ yr and $n = 25$ yr, Eq. (39) gives four reapplications, in years 5, 10, 15 and 20. The discounted cumulative cash flow turns positive in year 3 and reaches 0.045 million USD at the end of the project life, against 0.121 million USD in nominal terms.

Because the cash-flow series changes sign more than once, the internal rate of return is reported alongside the modified internal rate of return, 38.6% and 10.9% respectively at the reference layout, and the net present value is treated as the primary decision metric throughout (Section 3.5).

4.9. Comparison with reported values and limitations of the comparison

The energy gains obtained here fall within the range reported in the experimental literature for comparable albedo changes, and the functional forms, linear in treated albedo and concave in optimally ordered coverage, are consistent with both field measurement and independent simulation [15, 8, 17]. Direct numerical comparison with published studies is nevertheless of limited value, because reported bifacial gains depend on latitude, ground-coverage ratio, clearance height, mounting geometry, module bifaciality and the definition of gain adopted [15, 60], and no published study treats a spatially non-uniform ground albedo.

Four limitations bound the results specifically. The treatment is modelled as a first-reflection Lambertian surface, so a strongly specular product would deliver a different angular distribution and, in general, a smaller gain to an interior row than these results suggest. The energy model contains no inverter power limit, so the reported gains are not reduced by clipping and are upper bounds for a plant with a finite inverter rating. The reflectance decay trajectory and the vegetation-suppression fraction are inputs rather than model outputs, and the durability literature does not yet constrain either with the specificity the lifecycle analysis assumes; the sensitivities above are reported for that reason. Finally, the analysis is for a single fixed-tilt geometry at one site, and while the model applies without modification to tracking and vertical configurations, the balance between coverage and albedo found here should not be assumed to carry across to them.

5. Conclusions

Reflective ground treatment for bifacial photovoltaic plants has been assessed as a capital investment rather than as a fixed property of the site, using a view-factor irradiance model extended to a spatially varying ground albedo. The following conclusions are drawn.

1. The extension to non-uniform ground albedo is exact rather than approximate. Because the irradiance incident on a ground segment does not depend on that segment's reflectance, the transfer to the module is linear in the segment radiosities, so the spatially varying model reduces identically to the uniform-albedo reference formulation and inherits its verification. The same property makes the incremental irradiance exactly proportional to the albedo increment, which the implementation asserts as a numerical self-test and which yields the closed-form break-even reflectance of Eq. (50).

2. The model reproduces the published fixed-tilt bifacial benchmark to a normalised root-mean-square error of 0.026% on the front face and 0.108% on the rear, with no systematic sign, and reproduces eight months of measured monthly bifacial gain at Roskilde to a mean absolute error of 0.392 percentage points, seven of the eight months falling inside the ± 1 percentage point criterion adopted from the source study, with the annual value reproduced to 0.037 percentage points. The energy conversion agrees with an independent implementation to machine precision at equal cell temperature, and the financial equations reproduce five published cases. Annual energy has not been validated against a measured total, and that limit is stated rather than absorbed.
3. The ground is not uniformly worth treating. The annual rear-side response varies by a factor of 3.9 across the row pitch, being largest close to the rows where the view factor is greatest. 65% of the available benefit is obtainable from the first half of the ground area if the treatment is placed in descending order of response, against 50% for uniform application at the same cost.
4. Treatment cost scales strictly with area while the benefit is concave in coverage, so the value-maximising coverage is set by the ratio of unit cost to contract price. At 2.25 USD m^{-2} and 45 USD MWh^{-1} the last increment of ground still repays itself and net present value is flat above roughly 80% coverage, reaching 0.052 million USD at 90%, where the annual energy gain is 14.3% at an incremental levelised cost of 30.8 USD MWh^{-1} and an internal rate of return of 27.6%. A well-separated interior optimum emerges above a combined unit cost of roughly 3 USD m^{-2}, where the break-even reflectance at full coverage exceeds the reflectance the product delivers. Internal rate of return, by contrast, falls monotonically with coverage throughout, so the two metrics rank coverage differently and net present value is the appropriate criterion.
5. The energy gain is linear in treated albedo, in agreement with reported field measurements across concrete, soil and high-reflectance surfaces. The resulting break-even reflectance is 0.50 at full coverage and 0.36 for a narrow band alongside the rows, so reflectance and placement act as substitutes. Specifying the reflectance of the product is more consequential than specifying the area to be covered, and the treated region is better specified as a band adjacent to the rows than as a fraction of the site.
6. The case does not rest on energy alone. Avoided vegetation management contributes 8.4% of the treatment net present value at the reference assumptions, and is reported separately because a treatment justified principally by avoided mowing carries different durability requirements from one justified by rear-side irradiance gain.

Four limitations bound these conclusions. The treatment is modelled as a first-reflection Lambertian reflector, so a strongly specular product would distribute reflected radiation differently and, in general, deliver less to an interior row. The energy model contains no inverter power limit, so the reported gains are upper bounds for a plant with a finite inverter rating. The reflectance decay trajectory and the vegetation-suppression fraction are inputs rather than model outputs, and the durability literature does not yet constrain either with the specificity the lifecycle analysis assumes. Finally, the analysis covers one fixed-tilt geometry at one site; the formulation applies without modification to tracking and vertical configurations, but the balance between coverage and reflectance found here should not be assumed to carry across to them.

The natural extension is a field trial with a spatially non-uniform treatment and measured rear-side irradiance, which would validate the placement result directly. No such dataset is known to the authors, and its absence is the principal barrier to treating the optimal-placement result as established rather than as modelled.

Author Contributions

Muhammad Usama: Methodology, modeling, drafting, **Muhammad Abdullah Zafar Ghauri:** Drafting, data interpretation, **Jake Bendetti:** Conceptualization, financial model validation, **Moiz Ahmed Mahesar:** Financial model development, **Omer Emre Tunca:** Model validation, **Yetkin Yildirim:** Conceptualization.

Declaration of Competing Interest

The authors declare that they have no known competing financial interests or personal relationships that could have appeared to influence the work reported in this paper.

Declaration of generative AI use

Generative AI tools were used to provide guidance on developing the graphical abstract, and for evaluating the errors and marked divergence between `bifacialvf` and the model developed for this study.

Data Availability

The source code used for the modeling has been uploaded to GitHub and can be accessed at: https://github.com/Usama10345/Solar-bifacial-partial-ground-treatment-model.git.

References

[1] C. D. Rodríguez-Gallegos, H. Liu, O. Gandhi, J. P. Singh, V. Krishnamurthy, A. Kumar, J. S. Stein, S. Wang, L. Li, T. Reindl, I. M. Peters, Global techno-economic performance of bifacial and tracking photovoltaic systems, Joule 4 (2020) 1514–1541. URL: https://www.sciencedirect.com/science/article/pii/S2542435120301884. doi:https://doi.org/10.1016/j.joule.2020.05.005.

[2] R. O. Yakubu, L. D. Mensah, D. A. Quansah, M. S. Adaramola, A systematic literature review of the bifacial photovoltaic module and its applications, The Journal of Engineering 2024 (2024) e12421. URL: https://ietresearch.onlinelibrary.wiley.com/doi/abs/10.1049/tje2.12421. doi:https://doi.org/10.1049/tje2.12421. arXiv:https://ietresearch.onlinelibrary.wiley.com/doi/pdf/10.1049/tje2.12421.

[3] B. Marion, Measured and satellite-derived albedo data for estimating bifacial photovoltaic system performance, Solar Energy 215 (2021) 321–327. URL: https://www.sciencedirect.com/science/article/pii/S0038092X20313098. doi:https://doi.org/10.1016/j.solener.2020.12.050.

[4] S. Ayala Pelaez, C. Deline, S. M. MacAlpine, B. Marion, J. S. Stein, R. K. Kostuk, Comparison of bifacial solar irradiance model predictions with field validation, IEEE Journal of Photovoltaics 9 (2019) 82–88. doi:10.1109/JPHOTOV.2018.2877000.

[5] S. Ayala Pelaez, C. Deline, P. Greenberg, J. S. Stein, R. K. Kostuk, Model and validation of single-axis tracking with bifacial PV, IEEE Journal of Photovoltaics 9 (2019) 715–721. doi:10.1109/JPHOTOV.2019.2892872.

[6] A. C. J. Russell, C. E. Valdivia, C. Bohémier, J. E. Haysom, K. Hinzer, Duet: A novel energy yield model with 3-d shading for bifacial photovoltaic systems, IEEE Journal of Photovoltaics 12 (2022) 1576–1585. URL: https://api.semanticscholar.org/CorpusID:250296899.

[7] E. M. Tonita, A. C. Russell, C. E. Valdivia, K. Hinzer, Optimal ground coverage ratios for tracked, fixed-tilt, and vertical photovoltaic systems for latitudes up to 75°n, Solar Energy 258 (2023) 8–15. URL: https://www.sciencedirect.com/science/article/pii/S0038092X23002682. doi:https://doi.org/10.1016/j.solener.2023.04.038.

[8] E. M. Tonita, C. E. Valdivia, A. C. J. Russell, M. Martinez-Szewczyk, M. I. Bertoni, K. Hinzer, Quantifying spectral albedo effects on bifacial photovoltaic module measurements and system model predictions, Progress in Photovoltaics: Research and Applications 32 (2024) 468–480. URL: https://onlinelibrary.wiley.com/doi/abs/10.1002/pip.3789. doi:https://doi.org/10.1002/pip.3789. arXiv:https://onlinelibrary.wiley.com/doi/pdf/10.1002/pip.3789.

[9] A. F. Almarshoud, M. A. Abdel-halim, R. A. Almasri, A. M. Alshwairekh, Exergy and energy analysis of bifacial pv module performance on a cloudy day in saudi arabia, Sustainability 16 (2024). URL: https://www.mdpi.com/2071-1050/16/17/7428. doi:10.3390/su16177428.

[10] A. A. B. Baloch, S. Hammat, B. Figgis, F. H. Alharbi, N. Tabet, In-field characterization of key performance parameters for bifacial photovoltaic installation in a desert climate, Renewable Energy 159 (2020) 50–63. URL: https://www.sciencedirect.com/science/article/pii/S096014812030879X. doi:https://doi.org/10.1016/j.renene.2020.05.174.

[11] E.-M. Grommes, F. Schemann, F. Klag, S. Nows, U. Blieske, Simulation of the irradiance and yield calculation of bifacial pv systems in the usa and germany by combining ray tracing and view factor model, EPJ Photovolt. 14 (2023). URL: https://doi.org/10.1051/epjpv/2023003.

[12] S. Ghafiri, M. Darnon, A. Davigny, J. P. F. Trovão, D. Abbes, A comprehensive performance evaluation of bifacial photovoltaic modules: insights from a year-long experimental study conducted in the canadian climate, EPJ Photovolt. 15 (2024). URL: https://doi.org/10.1051/epjpv/2024025.

[13] A. Garrod, S. Neda Hussain, M. H. Intwala, A. Poudhar, S. Manikandan, A. Ghosh, Electrical and thermal performance of bifacial photovoltaics under varying albedo conditions at temperate climate (uk), Heliyon 10 (2024) e34147. URL: https://www.sciencedirect.com/science/article/pii/S2405844024101788. doi:https://doi.org/10.1016/j.heliyon.2024.e34147.

[14] X. Sun, M. R. Khan, C. Deline, M. A. Alam, Optimization and performance of bifacial solar modules: A global perspective, Applied Energy 212 (2018) 1601–1610. URL: https://www.sciencedirect.com/science/article/pii/S0306261917317567. doi:https://doi.org/10.1016/j.apenergy.2017.12.041.

[15] M. Alam, M. S. Gul, T. Muneer, Performance analysis and comparison between bifacial and monofacial solar photovoltaic at various ground albedo conditions, Renewable Energy Focus 44 (2023) 295–316. URL: https://www.sciencedirect.com/science/article/pii/S1755008423000066. doi:https://doi.org/10.1016/j.ref.2023.01.005.

[16] M. R. Lewis, S. Ovaitt, B. McDanold, C. Deline, K. Hinzer, Artificial ground reflector size and position effects on energy yield and economics of single-axis-tracked bifacial photovoltaics, Progress in Photovoltaics: Research and Applications 32 (2024) 675–686. URL: https://onlinelibrary.wiley.com/doi/abs/10.1002/pip.3811. doi:https://doi.org/10.1002/pip.3811. arXiv:https://onlinelibrary.wiley.com/doi/pdf/10.1002/pip.3811.

[17] N. Riedel-Lyngskær, P. B. Poulsen, M. L. Jakobsen, P. Nørgaard, J. Vedde, Value of bifacial photovoltaics used with highly reflective ground materials on single-axis trackers and fixed-tilt systems: a danish case study, IET Renewable Power Generation 14 (2020) 3946–3953. URL: https://ietresearch.onlinelibrary.wiley.com/doi/abs/10.1049/iet-rpg.2020.0580. doi:https://doi.org/10.1049/iet-rpg.2020.0580. arXiv:https://ietresearch.onlinelibrary.wiley.com/doi/pdf/10.1049/iet-rpg.2020.0580.

[18] S. Zainali, S. Ma Lu, B. Stridh, A. Avelin, S. Amaducci, M. Colauzzi, P. E. Campana, Direct and diffuse shading factors modelling for the most representative agrivoltaic system layouts, Applied Energy 339 (2023) 120981. URL: https://www.sciencedirect.com/science/article/pii/S0306261923003458. doi:https://doi.org/10.1016/j.apenergy.2023.120981.

[19] S. Ma Lu, S. Zainali, E. Sundström, A. Nygren, B. Stridh, A. Avelin, P. Campana, Validation of vertical bifacial agrivoltaic and other systems modelling: Effect of dynamic albedo on irradiance and power output estimations, AgriVoltaics Conference Proceedings 2 (2024). doi:10.52825/agripv.v2i.1004.

[20] H. A. Kazem, M. T. Chaichan, A. H. A. H. Al-Waeli, K. Sopian, Dual axis solar photovoltaic trackers: An in-depth review, Energy Sources, Part A: Recovery, Utilization, and Environmental Effects 46 (2024) 15331–15356. URL: https://doi.org/10.1080/15567036.2024.2420781. doi:10.1080/15567036.2024.2420781. arXiv:https://doi.org/10.1080/15567036.2024.2420781.

[21] S. Zainali, S. Ma Lu, B. Stridh, A. Avelin, P. Campana, 3d view factor power output modelling of bifacial fixed, single, and dual-axis agrivoltaic systems, AgriVoltaics Conference Proceedings 2 (2024). doi:10.52825/agripv.v2i.1003.

[22] D. Chudinzow, S. Nagel, J. Güsewell, L. Eltrop, Vertical bifacial photovoltaics – a complementary technology for the european electricity supply?, Applied Energy 264 (2020) 114782. URL: https://www.sciencedirect.com/science/article/pii/S0306261920302944. doi:https://doi.org/10.1016/j.apenergy.2020.114782.

[23] G. Badran, M. Dhimish, Comprehensive study on the efficiency of vertical bifacial photovoltaic systems: a uk case study, Scientific Reports 14 (2024) 18380. URL: https://doi.org/10.1038/s41598-024-68018-1. doi:10.1038/s41598-024-68018-1.

[24] O. H. AL-Zoubi, H. Al-Tahaineh, R. A. Damseh, A. H. AL-Zubi, A.-S. A. Odat, B. Shboul, Evaluating the real-world performance of vertically installed bifacial photovoltaic panels in residential settings: empirical findings and implications, International Journal of Low-Carbon Technologies 19 (2024) 386–442. URL: https://doi.org/10.1093/ijlct/ctad138. doi:10.1093/ijlct/ctad138. arXiv:https://academic.oup.com/ijlct/article-pdf/doi/10.1093/ijlct/ctad138/57199081/ctad1

[25] M. Bolinger, G. Bolinger, Land requirements for utility-scale pv: An empirical update on power and energy density, IEEE Journal of Photovoltaics 12 (2022) 589–594. doi:10.1109/JPHOTOV.2021.3136805.

[26] O. Ayadi, B. Rinchi, S. Al-Dahidi, M. E. B. Abdalla, M. Al-Mahmodi, Techno-economic assessment of bifacial photovoltaic systems under desert climatic conditions, Sustainability 16 (2024). URL: https://www.mdpi.com/2071-1050/16/16/6982. doi:10.3390/su16166982.

[27] F. Mandys, M. Chitnis, S. R. P. Silva, Levelized cost estimates of solar photovoltaic electricity in the united kingdom until 2035, Patterns 4 (2023) 100735. URL: https://www.sciencedirect.com/science/article/pii/S2666389923000752. doi:https://doi.org/10.1016/j.patter.2023.100735.

[28] S. Chen, X. Lu, J. Hao, E. Virgüez, K. Caldeira, S. J. Davis, The effect of land costs on the economic and sustainability performance of solar photovoltaics in china, Proceedings of the National Academy of Sciences 123 (2026) e2512930123. URL: https://www.pnas.org/doi/abs/10.1073/pnas.2512930123. doi:10.1073/pnas.2512930123. arXiv:https://www.pnas.org/doi/pdf/10.1073/pnas.2512930123.

[29] M. Ahmad, A. Khattak, A. Kashif Janjua, A. A. Alahmadi, M. Salman Khan, N. Ullah, Techno-economic feasibility analyses of grid- connected solar photovoltaic power plants for small scale industries of punjab, pakistan, Frontiers in Energy Research Volume 10 - 2022 (2022). URL: https://www.frontiersin.org/journals/energy-research/articles/10.3389/fenrg.2022.1028310. doi:10.3389/fenrg.2022.1028310.

[30] M. I. Hossain, A. Ali, V. Bermudez Benito, B. Figgis, B. Aïssa, Anti-soiling coatings for enhancement of pv panel performance in desert environment: A critical review and market overview, Materials 15 (2022). URL: https://www.mdpi.com/1996-1944/15/20/7139. doi:10.3390/ma15207139.

[31] A. Taquichiri, D. Olivares, A. Marzo, F. Valencia, F. M. Galleguillos-Madrid, M. Gaete, E. Fuentealba, Soiling dynamics and cementation in bifacial photovoltaic modules under arid conditions: A one-year study in the atacama desert, Energies 18 (2025). URL: https://www.mdpi.com/1996-1073/18/18/4999. doi:10.3390/en18184999.

[32] C. Molto, J. Oh, F. I. Mahmood, M. Li, P. Hacke, F. Li, R. Smith, D. Colvin, M. Matam, C. DiRubio, G. Tamizhmani, H. Seigneur, Review of potential-induced degradation in bifacial photovoltaic modules, Energy Technology 11 (2023) 2200943. URL: https://onlinelibrary.wiley.com/doi/abs/10.1002/ente.202200943. doi:https://doi.org/10.1002/ente.202200943. arXiv:https://onlinelibrary.wiley.com/doi/pdf/10.1002/ente.202200943.

[33] B. Marion, S. MacAlpine, C. Deline, A. Asgharzadeh, F. Toor, D. Riley, J. Stein, C. Hansen, A practical irradiance model for bifacial pv modules, in: 2017 IEEE 44th Photovoltaic Specialist Conference (PVSC), 2017, pp. 1537–1542. doi:10.1109/PVSC.2017.8366263.

[34] J. Appelbaum, The role of view factors in solar photovoltaic fields, Renewable and Sustainable Energy Reviews 81 (2018) 161–171. URL: https://www.sciencedirect.com/science/article/pii/S1364032117310924. doi:https://doi.org/10.1016/j.rser.2017.07.026.

[35] R. Perez, P. Ineichen, R. Seals, J. Michalsky, R. Stewart, Modeling daylight availability and irradiance components from direct and global irradiance, Solar Energy 44 (1990) 271–289. URL: https://www.sciencedirect.com/science/article/pii/0038092X9090055H. doi:https://doi.org/10.1016/0038-092X(90)90055-H.

[36] N. Martin, J. Ruiz, Calculation of the pv modules angular losses under field conditions by means of an analytical model, Solar Energy Materials and Solar Cells 70 (2001) 25–38. URL: https://www.sciencedirect.com/science/article/pii/S0927024800004086. doi:https://doi.org/10.1016/S0927-0248(00)00408-6.

[37] J. A. Duffie, W. A. Beckman, Solar Engineering of Thermal Processes, 4th ed., John Wiley & Sons, Hoboken, NJ, 2013. doi:10.1002/9781118671603.

[38] W. Short, D. Packey, T. Holt, A Manual for the Economic Evaluation of Energy Efficiency and Renewable Energy Technologies, Technical Report NREL/TP-462-5173, National Renewable Energy Laboratory, 1995. doi:10.2172/35391.

[39] R. Brealey, S. Myers, F. Allen, Principles of Corporate Finance, The Irwin/McGraw-Hill series in finance, insurance, and real estate, McGraw-Hill Education, 2016.

[40] C. Deline, S. Ovaitt, M. Mikofski, bifacialvf: Bifacial pv view factor model, 2026. URL: https://doi.org/10.5281/zenodo.20804569. doi:10.5281/zenodo.20804569.

[41] R. Perez, R. Stewart, R. Seals, T. Guertin, The development and verification of the Perez diffuse radiation model, Technical Report, Sandia National Labs., Albuquerque, NM (USA); State Univ. of New York, Albany (USA). Atmospheric Sciences Research Center, 1988. URL: https://www.osti.gov/biblio/7024029. doi:10.2172/7024029.

[42] N. Martín, J. M. Ruiz, A new model for pv modules angular losses under field conditions, International Journal of Solar Energy 22 (2002) 19–31. URL: https://doi.org/10.1080/01425910212852. doi:10.1080/01425910212852. arXiv:https://doi.org/10.1080/01425910212852.

[43] National Renewable Energy Laboratory, Typical meteorological year 3 weather data: Dallas-fort worth international airport, texas, wmo 722590, 2008. URL: https://github.com/NatLabRockies/resstock/blob/develop/resources/hpxml-measures/weather/USA_TX_Dallas-Fort.Worth.Intl.AP.722590_TMY3.epw, hourly TMY3 weather file; latitude 32.90 degrees N, longitude 97.02 degrees W, elevation 171 m; period of record 1973-2005.

[44] S. Wilcox, W. Marion, Users Manual for TMY3 Data Sets, Technical Report NREL/TP-581-43156, National Renewable Energy Laboratory, 2008. doi:10.2172/928611.

[45] JinkoSolar, Jkm605-630n-66hl4m-bdv: 605-630 watt bifacial module with dual glass, Manufacturer datasheet, 2024. URL: https://jinkosolarcdn.shwebspace.com/uploads/JKM605-630N-66HL4M-BDV-F3-EN.pdf.

[46] PV Performance Modeling Collaborative, Albedo, ???? URL: https://pvpmc.sandia.gov/modeling-guide/1-weather-design-inputs/plane-of-array-poa-irradiance/calculating-poa-irradiance/poa-ground-reflected/albedo/, typical grass albedo reported as 0.15-0.25.

[47] M. Usama, Z. Ali, M. C. Ndukwu, R. Sathyamurthy, The energy, emissions, and drying kinetics of three-stage solar, microwave and desiccant absorption drying of potato slices, Renewable Energy 219 (2023) 119509. URL: https://www.sciencedirect.com/science/article/pii/S0960148123014246. doi:https://doi.org/10.1016/j.renene.2023.119509.

[48] V. Ramasamy, J. Zuboy, D. Feldman, M. Narayanaswami, M. Woodhouse, R. Margolis, Documenting 15 Years of Reductions in U.S. Solar Photovoltaic System Costs, Technical Report NREL/TP-7A40-92536, National Renewable Energy Laboratory, Golden, CO, 2025. URL: https://www.nrel.gov/docs/fy25osti/92536.pdf.

[49] A. P. Dobos, PVWatts Version 5 Manual, Technical Report NREL/TP-6A20-62641, National Renewable Energy Laboratory, Golden, Colorado, 2014. URL: https://doi.org/10.2172/1158421. doi:10.2172/1158421.

[50] R. Clark, J. Eudave, Boosting bifacial panel efficiency with albedo ground covers: Field test results, PV Magazine, 2021. URL: https://www.pv-magazine.com/2021/02/01/boosting-bifacial-panel-efficiency-with-albedo-ground-covers-field-test-results/, industry case study.

[51] J. McCall, J. Macdonald, R. Burton, J. Macknick, Vegetation management cost and maintenance implications of different ground covers at utility-scale solar sites, Sustainability 15 (2023) 5895. URL: https://doi.org/10.3390/su15075895. doi:10.3390/su15075895.

[52] J. Seel, J. Mulvaney Kemp, A. Cheyette, W. Gorman, N. R. Darghouth, D. Robson, J. Rand, S. Jeong, U.s. utility-scale solar, 2025 data update, Lawrence Berkeley National Laboratory, 2025. URL: https://eta-publications.lbl.gov/publications/us-utility-scale-solar-2025-data.

[53] Federal Open Market Committee, 2025 statement on longer-run goals and monetary policy strategy, Board of Governors of the Federal Reserve System, 2025. URL: https://www.federalreserve.gov/monetarypolicy/monetary-policy-strategy-tools-and-communications-statement-on-longer-run-goals-monetary.htm.

[54] Lazard, Lazard's levelized cost of energy analysis, version 17.0, https://www.lazard.com, 2024.

[55] K. S. Anderson, C. W. Hansen, W. F. Holmgren, A. R. Jensen, M. A. Mikofski, A. Driesse, pvlib python: 2023 project update, Journal of Open Source Software 8 (2023) 5994. doi:10.21105/joss.05994.

[56] D. Faiman, Assessing the outdoor operating temperature of photovoltaic modules, Progress in Photovoltaics: Research and Applications 16 (2008) 307–315. doi:10.1002/pip.813.

[57] L. Narvarte, E. Lorenzo, Tracking and ground cover ratio, Progress in Photovoltaics: Research and Applications 16 (2008) 703–714. doi:10.1002/pip.847.

[58] S. Ong, C. Campbell, P. Denholm, R. Margolis, G. Heath, Land-Use Requirements for Solar Power Plants in the United States, Technical Report NREL/TP-6A20-56290, National Renewable Energy Laboratory, 2013. doi:10.2172/1086349.

[59] H. L. Tan, B. H. Lim, M. H. Tan, X. Zeng, K.-K. Chong, K. H. Chua, Y. Zhang, Investigation of bifacial gain and albedo of bifacial photovoltaic modules that operate in a tropical site, in: 2024 8th International Conference on Green Energy and Applications (ICGEA), 2024, pp. 265–270. doi:10.1109/ICGEA60749.2024.10560565.

[60] M. Kivambe, A. Abdallah, D. Pillai, M. Abdelrahim, M. Elgaili, The impact of module technology, ground coverage ratio, and string configuration on the performance of bifacial pv systems on horizontal single-axis trackers in desert environments, Renewable Energy 269 (2026) 125855. URL: https://www.sciencedirect.com/science/article/pii/S0960148126006816. doi:https://doi.org/10.1016/j.renene.2026.125855.

Introduction to Problem:

The solar market is actively moving to embrace bifacial solar panel technology. But to realize maximum gain of the second side or the back side of solar panels, many external variables need to be in place, including the 1) reflectivity of smooth freshly fallen snow, 2) best time of day, 3) best geographic location, 4) module mounting height, 5) most effective tilting of the solar array and a few others.

This reflectivity AND smoothness (of freshly fallen snow) is measured with an albedometer and prior studies have indicated that the ground must have an albedo of 0.8 or higher to assist in maximum gain.

From our conversations with numerous bifacial panel users, it appears that many do not clearly understand the foregoing. Developers are investing in bifacial technology without the assurance that gains (often stated by bifacial panel manufacturers on their product technical data sheets with specific percentages) are possible. Albedo is the fraction of light reflected from the surface. So, because a manufacturer states that the second side of a bifacial panel is capable of ~25% gain increase, that gain cannot be guaranteed without the five external variables mentioned above.

To approximate freshly fallen snow, we have spoken to many developers who have considered and tested these materials:

1. White Gravel or Rock

Because some white rock is inconsistently colored, the albedo might be less consistent. When maintenance vehicles drive over white gravel, their tires will tend to disburse the rocks which may "fly" and other rocks will be pushed further into the soil. So, at some point, additional white gravel or rock may have to be delivered. White gravel or rock can cost $17-$20/sqm

2. White Agricultural Fabric

While white fabric agricultural ground cover is an option, it will not last for 30 years. White specialty fabric can cost $5 per sqm. Costs do not factor in installation and maintenance cost.

In 2019, Burns McDonnel shared the following in their white paper “Bifacial Modules” authored by Will Porter:

“Albedo — Annual energy production increases of 5% to 10% are typical with bifacial modules. In most areas, imported groundcover is often needed to push the increase much over 10%. The question is, does it pay to bring in light-colored gravel or roofing to control albedo? The answer to this question is both location- and project-specific, and a cost evaluation is needed to make the final determination. The estimated albedo for various surfaces is outlined in Figure 2.”

In turn, Burns McDonnel referenced this albedo test from SolarWorld:

Green field / grass	23
Concrete	16
White painted concrete	60-80
White gravel	27
White roofing material	56
Light gray roofing foil	62
White roofing foil for solar	>80

Center photo: **This installation does not exist.** This picture has been retouched using Photoshop so one can see a proposed installation of soil stabilizer on a fixed tilt system.

Simulate freshly fallen snow for 30 continuous years.

Leverage bifacial solar panel technology in solar farms.

www.terrapavetech.com info@terrapavetech.com

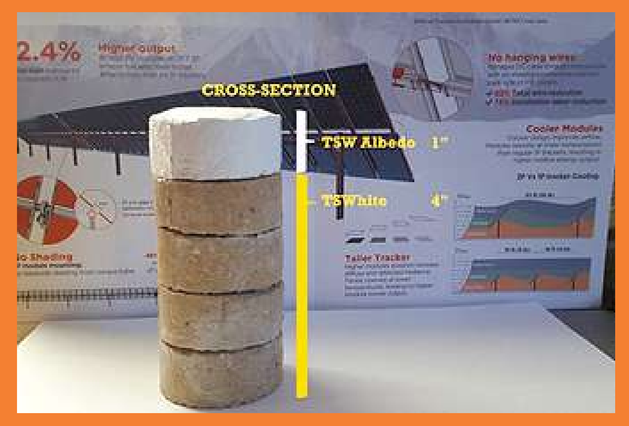


Methods (experimental design, techniques)

Texas-based Eco Estates International, in conjunction with the University of Texas worked to create a liquid soil stabilizer that permanently binds and transforms the ground into a concrete-pavement-like-layer and 100% eco-friendly.

When sprayed on prepared soil, the soil stabilizer changes the color of the ground and achieves the albedo of snow. The soil stabilizers are proprietary polymer-based emulsions that use water dilutions non-toxic for the application process.

Fundamentally, the soil stabilizer represents a highly sophisticated piece of “equipment”.



The higher the albedo of the surface under your bifacial panel, the more gain you can realize from your bifacial panel. The darker the surface under your bifacial panel, you will not be able to realize the complete ~25% UNLESS you have the albedo of smooth fresh fallen snow which is 0.80 to 0.90. We believe this soil stabilizer can give the ground a permanent, consistent and highly reflective surface.

We believe it will solve the albedo problem and provide easier financial modeling, accurate engineering design and accurate prediction for bifacial panels.



As Asphalt roads are not eco-friendly and their construction comes with the generation of toxic fumes and high costs, we believe this soil stabilizer will enable the creation of much less expensive, eco-friendly access roads to reach a solar farm.



Because the soil stabilizer behaves as pavement, we believe it will block vegetation growth where it is applied: possible savings in maintenance costs might result.

Because the soil stabilizer behaves as pavement, it can reduce Shading Loss. Therefore, a possible increase in power generation might result.

